A study on detailing gusset plate and bracing members in concentrically braced frame structures

M.S. Hassan[1,2], S. Salawdeh[1,2], A. Hunt[3], B.M. Broderick[4] and J. Goggins[1,2*]

[1]*Civil Engineering, School of Engineering, National University of Ireland Galway, Ireland*
[2]*MaREI Centre for Marine and Renewable Energy Ireland, Ryan Institute, National University of Ireland Galway, Ireland*
[3]*AECOM, St Albans, United Kingdom*
[4]*Department of Civil, Structural & Environmental Engineering, Trinity College Dublin, Ireland*

Abstract. Conventional seismic design of concentrically braced frame (CBF) structures suggests that the gusset plate connecting a steel brace to beams and/or columns should be designed as non-dissipative in earthquakes, while the steel brace members should be designed as dissipative elements. These design intentions lead to thicker and larger gusset plates in design on one hand and a potentially under-rated contribution of gusset plates in design, on the other hand. In contrast, research has shown that compact and thinner gusset plates designed in accordance with the elliptical clearance method rather than the conventional standard linear clearance method can enhance system ductility and energy dissipation capacity in concentrically braced steel frames. In order to assess the two design methods, six cyclic push-over tests on full scale models of concentric braced steel frame structures were conducted. Furthermore, a 3D finite element (FE) shell model, incorporating state-of-the-art tools and techniques in numerical simulation, was developed that successfully replicates the response of gusset plate and bracing members under fully reversed cyclic axial loading. Direct measurements from strain gauges applied to the physical models were used primarily to validate FE models, while comparisons of hysteresis load-displacement loops from physical and numerical models were used to highlight the overall performance of the FE models. The study shows the two design methods attain structural response as per the design intentions; however, the elliptical clearance method has a superiority over the standard linear method as a fact of improving detailing of the gusset plates, enhancing resisting capacity and improving deformability of a CBF structure. Considerations were proposed for improvement of guidelines for detailing gusset plates and bracing members in CBF structures.

Keywords: seismic design; concentrically braced frames; steel structures; earthquake engineering; gusset plates; steel hollow sections; finite element modelling

1. Introduction

Concentrically braced frame (CBF) steel structures, in which the diagonal members intersect the centre line of beams and columns, forms one of the most effective systems for providing

---

∗Corresponding author, Ph.D. E-mail: jamie.goggins@nuigalway.ie

seismic resistance in both low- and high-rise buildings. They resist build-up forces during earthquakes by vertical in plane truss mechanisms consisting of alternating compression and tension forces in the bracing members. In strong earthquakes, however, these bracing members can be subjected to limit states, such as local buckling and fracture. As a result, the key focus of earlier research was mainly on investigating the cyclic axial response of steel braces (Tremblay 2002, Goggins 2004, Haddad *et al*. 2004, Goggins *et al*. 2006, Goggins and Salawdeh 2013, Haddad 2015, Ryan *et al*. 2017). It was generally concluded that global and local slenderness were two important parameters influencing the local buckling and fracture. Consequently, slenderness limits were proposed in detailing bracing members to obtain better fatigue lives during earthquakes.

More recently, interest has shifted to examination of details influencing gusset plate behaviour in CBF structures. Gusset plates are a structurally efficient means of connecting steel braces with beams and columns of the CBF, but their design must accommodate the unique hysteretic response behaviour of the steel braces. However, there is a lack of sufficient guidance on detailing and dimensioning of the gusset plates in CBF structures, primarily due to absence of relevant data in the literature. To regulate the design process, Eurocode 8 (EC8) (CEN 2004) suggests detailing of gusset plates in accordance with available methods or accompanied with experimental evidence in the absence of a suitable method. Physical laboratory tests can be time consuming, difficult and costly. To avoid this hindrance, structural engineers typically use established design methods available. Of them, the Standard Linear Clearance (SLC) method is one of the most commonly used due to its simplicity and ease. This method, however, neglects important seismic effects due to bracing steel members and frame actions both in plane and out-of-plane (Bjorhovde and Chakrabarti 1985, Hu and Cheng 1987, Brown 1989, Cheng *et al*. 1994). As a result, the ability of this method to develop and predict the performance of test models of CBF under realistic earthquake loading was found to be poor and was below the required performance (Lehman *et al*. 2008). In addition, it has been established that the method leads to gusset plates that are typically thick, large and not the most cost-effective solution. On the other hand, a balanced design approach, in which the non-linear off-set rule or so called Elliptical Clearance (EC) method is used to balance the tensile yield resistances of the structural steel brace and gusset plate (Lehman *et al*. 2008). Salient features of the two design philosophies are highlighted in Table 1.

It is widely accepted that CBF structures display attractive stiffness and strength under low to moderate magnitude earthquakes but can perform less favourably in strong earthquakes compared to some alternative structural systems (for example, moment resisting frames (MRF)) due to possessing lower ductility and less energy absorption capabilities. With the aid of improved gusset plate design, these deficiencies can be overcome in CBF structures. The relative stiffness of the gusset plate compared to the brace member will influence the location and extent of buckling in the system.

This paper provides essential information on the balanced design approach and investigates the performance of this method relative to the conventional design approach, which is currently used by structural engineers. Realistic gusset plate details and bracing members were used to generate experimental data. This experimental data is utilised into a finite element framework to develop models of test specimens. The paper is a part of a larger research project (Broderick *et al*. 2015, Salawdeh *et al*. 2017, Goggins *et al*. 2018) that investigates the influence of various gusset plate details with bracing members on the inelastic response of CBF structures under earthquakes. In this paper, the inelastic cyclic behaviour of brace gusset-plate members is studied with the aid of finite element models. In particular, the fatigue performance of the models in relation to standardised seismic design methods for brace gusset-plate members are investigated. The models'

Table 1 Comparison of two gusset plate design philosophies

Elliptical Clearance (EC) design	Standard Linear Clearance (SLC) design
✓ Both brace and gusset plate evolve system performance.	✓ Braces mainly derive system performance.
✓ Gusset plate may experience inelastic strains during brace tension.	✓ Gusset plate remains elastic during brace tension.
✓ The β_{ww} ratio characterises the balance of the brace and gusset plate yielding mechanisms.	✓ No such sharing mechanisms exist for this system.
✓ The deformation of the system is shared by two elements during seismic action.	✓ During seismic action, brace usually suffer inelastic deformations.
✓ Gusset plate has dual role in this system, (i) it accommodates brace end rotation, (ii) contributes in ductility and energy dissipation capacity and increases brace fatigue-life.	✓ Gusset plate has a single role in this system that is to accommodate brace end rotation.
✓ Thinner and compact gusset plates provide reduced structural cost of dissipative members.	✓ Uneconomical, larger and thicker gusset plate typically arise.
✓ Weak gusset plates reduce probability of hinge formation at joints formed by beam-column by engaging themselves instead.	✓ Large gusset plates remain stiff and strong during seismic action and facilitate formation of plastic hinges at joints formed by beam and column non-dissipative members.

predictions are compared to physical quasi-static tests conducted in the laboratory. The performance of the models is evaluated in terms of initial yield strength, initial-post buckling compressive strength, ductility capacity, energy dissipation capacity, number of cycles to global and local buckling and fatigue capacity.

2. Physical laboratory test

Hunt (2013) carried out quasi-static tests on full scale models of a single storey plane CBF structure. Six brace gusset-plate specimens designed with realistic structural details were tested in a displacement-controlled set-up. These specimens were tested as part of a CBF structure to accurately represent realistic boundary conditions. The scope of the tests includes specimens that have following specifications:
  • Brace section size
  o   S40   40x40x2.5 (mm)
  o   S60   60x60x2.5 (mm)
  • Connection configuration
  o   CA   Gusset connection to beam and column flange
  o   CB   Gusset connection to beam only
  • Gusset plate design
  o   G1   Conventional design with Standard Linear Clearance (SLC)
  o   G2   Balanced design with Elliptical Clearance (EC)
The brace slenderness ratios were determined in accordance with Eurocode 3 (EC3) (CEN 1993) guidelines and covers the broad range of allowable steel braces permitted by EC8 (CEN 2004) for braced steel frames structures that is $\bar{\lambda} \leq 2.0$. Also, all braces were designated as Class 1 cross-sections as per EC3 (CEN 1993). Rectangular gusset plates were used with four cross-section sizes, identified as (l_h x l_v x t_p), of 285x240x8, 270x230x4, 265x240x8 and 250x230x4mm.

Table 2 Summary of test models (Hunt 2013)

Specimen	Brace section size	Connection type	Gusset plate clearance	t_p (mm)	b_w (mm)	I_h (mm)	I_v (mm)	Brace length, L_b (mm)	β_{ww}
S40-CA-G1	40x40x2.5	CA	SLC ($3t_p$)	8	155	285	240	2368	0.38
S40-CA-G2	40x40x2.5	CA	EC ($8t_p$)	4	155	270	230	2503	0.75
S40-CB-G1	40x40x2.5	CB	SLC ($3t_p$)	8	155	265	240	2368	0.38
S40-CB-G2	40x40x2.5	CB	EC ($8t_p$)	4	155	250	230	2503	0.75
S60-CA-G1	60x60x2.5	CA	SLC ($3t_p$)	8	175	285	240	2368	0.52
S60-CA-G2	60x60x2.5	CA	EC ($8t_p$)	4	175	270	230	2467	1.03

The specific details of the gusset plates are given in Table 2 and Fig. 1. All specimens are classified as G1 or G2 as per the two design methods for the gusset plates; G1 refers to the specimen which is designed as per the conventional design approach, in which the linear off-set rule or so called Standard Linear Clearance (SLC) method was used to design the gusset plate and G2 refers to the specimen which is designed as per the balanced design approach, in which the non-linear off-set rule or so called Elliptical Clearance (EC) method is used (Fig. 1). The difference between the design approaches lies in the fact that the former design approach supports thicker and larger gusset plates to accommodate brace end rotation, while the latter supports thinner and compact gusset plates to attain gusset plate yielding proportional to the yielding of brace element in tension and, to accommodate brace end rotation in compression. This proportional yielding, which is inter-related with yielding of bracing members, formed the basis of a design approach known as the balanced approach (Lehman *et al.* 2008). In this approach, the primary yielding mechanism is carried by brace action, while the secondary mechanisms by gusset plate action. The ratio, which is defined as β_{ww}, of the yield resistances of the two mechanisms determines the allowable proportional yielding between the two elements in accordance with properties associated with the geometry and material strength of steel braces and gusset plates, as

$$\beta_{ww} = \frac{R_{y,brace}F_yA_{net,brace}}{R_{y,gusset}F_{y,gusset}b_wt_p} \tag{1}$$

where R_y is the ratio of the actual yield stress to the nominal yield stress of steel material, F_y is the yield capacity of brace, $A_{net,brace}$ is the net brace area effective for gusset plate connection, b_w and t_p are the width and thickness of the gusset plate, respectively and the $F_{y,gusset}$ is the yield capacity of gusset plate.

EC8 (CEN 2004) does not provide strong rules on the detailing of gusset plate connections connecting steel braces with beams and columns in the CBF. Hence, two types of detailing connections were used in tests, one with the brace gusset plate connected to the beam only, denoted as CB and the other with the gusset plate connected to both the beam and column, denoted as CA. In Table 2, specimens are identified by the size of the brace, either S40 or S60, gusset plate connecting detail with beam and column as CA, or with only beam as CB and the gusset plate design as G1 or G2, including sequential number 1, 2 etc. The variable "b_w" is the Whitmore width, which is a function of weld length and width of brace section. The corresponding ratio β_{ww} was calculated in accordance with Lehman *et al.* (2008). All specimens were tested on a plane CBF structure supported by pinned end connections, as shown in Fig. 2.

(a) S40-CA-G1   (b) S40-CA-G2   (c) S40-CB-G1

(d) S40-CB-G2   (e) S60-CA-G1   (f) S60-CA-G2
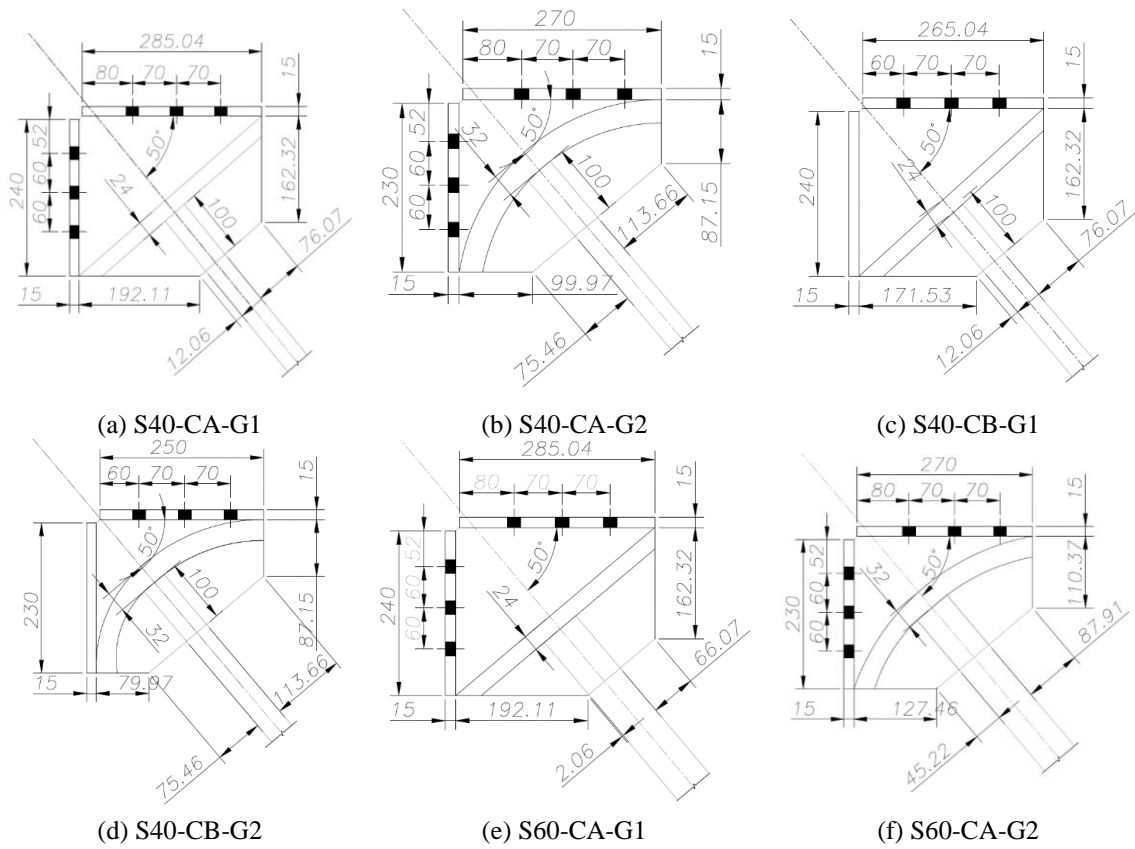
Fig. 1 Detailing of gusset plates in test models
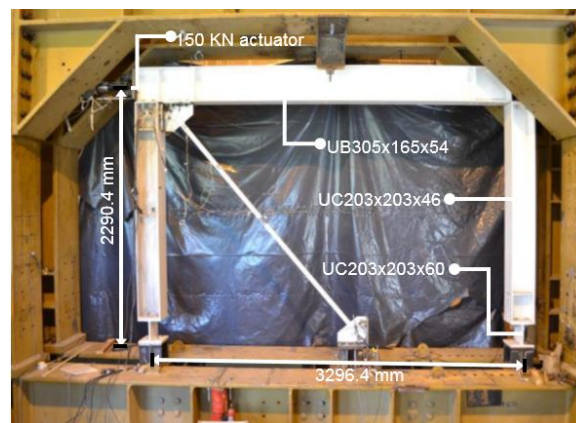
Fig. 2 Test set-up, including frame details

2.1 Loading protocol

The specimens involved in this study are particularly designed for seismic regions where they may undergo large inelastic strains causing fatigue in less than thirty cycles of loading. A loading
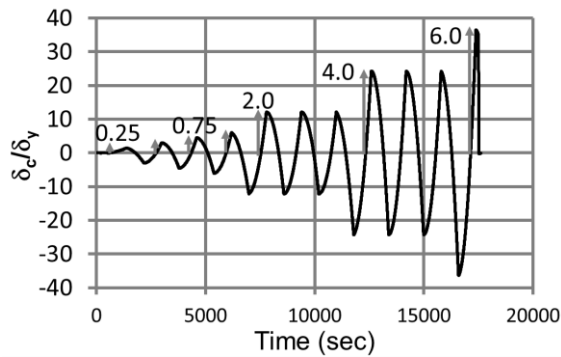
Fig. 3 Profile of loading protocol in accordance with ECCS (1986) guidelines
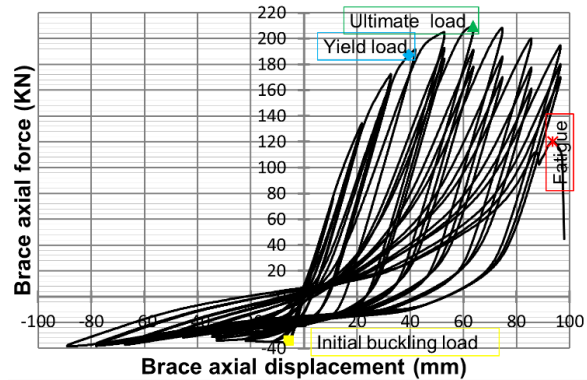
Fig. 4 Plot of hysteresis loops obtained from test model of S40-CB-G2-4 specimen

protocol that can develop such a large plastic strain in compression and tension periods was required. In this context, the ECCS (ECCS 1986) recommended cyclic protocol was employed. This protocol implies using one cycle of symmetric displacement magnitude of 0.25, 0.5, 0.75 and $1\delta_y$, follow by three cycles of displacement magnitudes of 2, 4, 6 δ_y, etc., where δ_y is the yield displacement (Fig. 3). The loading was applied uniaxially at the joint formed by the beam and column members with the aid of a hydraulic actuator (Fig. 2).

2.2 Hysteretic behaviour

A brief description on the response of specimen to ultra-low cycle fatigue loading is presented. Fig. 4 shows that the response of the specimen is non-symmetric, but essentially elastic for initial cycles of loading. The first major event is global buckling and the load corresponding to it is labelled with initial buckling load.

After occurrence of global buckling, axial compressive strength degraded as plastic rotation demand increases at mid-length brace tube. Further strength reduction occurs when identical loading magnitude is applied as a result of out-of-the-plane deformation and to a lesser extent due to the Baushinger effect. At each tensile excursion, permanent elongation occurs in the specimen, which upon load reversal causes additional thrust in compression and, thereby, the effect of U-shaped pinching occurs. The effect of U-shape pinching varies with the global slenderness ratio; the lower is the ratio of global slenderness, the earlier is the local buckling and the resulting U-shaped pinching effect in the brace buckling behaviour, provided that the section has a low width-to-thickness ratio. All braces were deemed as Class 1 cross-sections (CEN 1993) with intermediate global slenderness properties. Formation of local buckles in plastic hinges occurred initially at corners of the brace tube mid-length under compression loading. On the tension side, the maximum force resisted by specimen is marked with ultimate load in Fig. 4. The label "fatigue" indicates the point where the specimens had fractured in the physical test.

3. Finite element modelling framework

The numerical models were developed in ABAQUS v.6.13 (ABAQUS 2013), which is a general-purpose commercial finite element package. In order to give simplicity and ease to

modelling, two assumptions were made:

(i)   Connection between the gusset plate and frame has infinite stiffness (fully rigid).

(ii) The testing/supportive frame has negligible influence on cyclic response of the brace specimen.

3.1 Material model

Material modelling is a complex task when dealing with two components having different nominal yield strengths and fabrication processes. As such, the gusset plates are typically fabricated from hot-rolled carbon steel material, while the steel braces considered in this study were cold-formed carbon steel. Cyclic loading was employed in this study, which has two important effects on the behaviour of steel material; (i) cycling hardening of the material in tension and (ii) reducing yield strength in compression (Baushinger effect). A material model capable of representing two-cyclic strength degradation phenomenon was required. To this end, three material models were reviewed;

(i)   combined orthotropic kinematic hardening model,

(ii) isotropic hardening model,

(iii) combined nonlinear isotropic/kinematic hardening model.

Briefly, the combined orthotropic-kinematic hardening model tends to model elasticity of steel by mechanics of orthotropic material in which properties of a material are investigated in three dimensions. As such, the material response differs in three stress space. To solve this, the Hill criterion [21] (expansion of von Mises criterion) is employed for predicting yield strength of material in relation to properties of the material in the three axes. The condition of the two-symmetry plane must be satisfied at the points of integration to meet orthotropic criterion. Composites and/or brittle material typically exhibit such behaviour and, hence, it is suited to them. Steel behaves similar to an isotropic-like material, in which properties remain unchanged in all three-space configurations. Indeed, isotropy of steel can be modelled as orthotropic but with the expense of nine elastic constants, which requires extensive knowledge and tedious amount of work for accurate quantification. In conjunction, a kinematic hardening model is used to model shifting of a yield surface while loading material cyclically. In this way, the two models work collectively into a unified format. Upon application, it has produced an acceptable hysteresis loop of steel braces (see, for example, Haddad *et al*. (2004)).

In contrast, the isotropic elastic and hardening model requires two elastic constants to model the elasticity of a steel material. These elastic constants are the modulus of elasticity, E and the Poisson ratio, υ. The model considers inelastic response of material as isotropic on account of hardening. Hence, it neglects the contribution of Baushinger effect. Constitutively, a von Mises criterion, which is differentiable over the yielding surface, along with associative plastic flow rule is used to model hardening of steel. Upon application, hysteresis loops obtained from this model were found to be moderately non-representative of physical test data (see, for example, English and Goggins (2012)). The reason behind non-representation was associated to the limitation (stationery expansion and contraction) of the model. This limitation was overcome by using a combined nonlinear isotropic/kinematic hardening model. With this model, hardening of material can be modelled in both isotropic and kinematic states using the work of Lemaitre and Chaboche (1986) and the flow rule of plasticity. It has two important components; one is associated with isotropic hardening capturing the size of the yield surface as a function of plastic strain, while the second is associated with the kinematic component capturing shifting of a yield surface through

(a) test model

(b) FE model incorporated with Nip *et al.* (2010) parameters

(c) FE model incorporated with Fell (2008) parameters
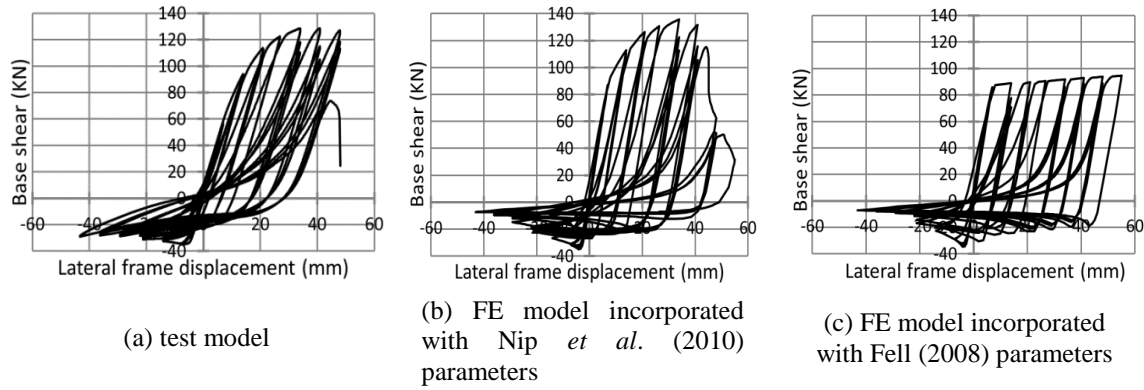
Fig. 5 Plots of base shear versus lateral frame displacement

Table 3 Material model for steel braces and gusset plates

Structural element	Cyclic hardening parameters			Kinematic shifting parameters		
	$\sigma\vert_o$	Q_∞	b_{iso}	$\sigma\vert_o$	C_{kin}	γ
	MPa	MPa		MPa	MPa	
All steel braces	Table 6	32.9	0.133	Table 3	87100	394
All gusset plates	Table 6	87	1.5	Table 3	30200	188

back-stress variable known as the Baushinger variable. The two components work collectively and should be defined as part of a bulk material property. Each component has three non-linear parameters defined accordingly (ABAQUS 2013) as:

- Isotropic hardening parameters:
  - $\sigma\vert_o$ It is the yield stress at zero equivalent plastic strain
  - C_{kin} It is the kinematic hardening parameter
  - γ It determines the rate at which the back stresses vary as the plastic strain increases.
- Kinematic hardening parameters:
  - $\sigma\vert_o$ It is the yield stress at zero equivalent plastic strain
  - b_{iso} It is the hardening parameter that defines the rate at which the size of the yield surface changes as plastic strain increases
  - Q_∞ It defines the maximum change in the size of the yield surface

Hunt (2013) carried out tests on coupons of gusset plates and steel braces under static tensile loading. This set of coupon test were used to establish the yield strength. The modelling parameters proposed by Nip *et al.* (2010) and Fell (2008) for hot-rolled carbon steel and cold-formed carbon steel material in relation to combined nonlinear isotropic and kinematic hardening model were assessed by simulating initial runs of the finite element model for specimen S40-CB-G1-3. It was found that the Fell (2008) model did not accurately predict the strain hardening response of the brace, which was accurately modelled by Nip *et al.* (2010), as shown in Fig. 5. It was also found that by changing parameters of the Fell (2008) model and the Nip *et al.* (2010) model for hot-rolled gusset-plate steel material, while keeping properties of the cold-formed bracing members from Nip *et al.* (2010) model, the response of the FE model did not alter significantly. Hence, the Nip *et al.* (2010) model was adopted with parameters corresponding to 40x40x2.5mm cold-formed brace steel member (Table 3). In the absence of measured data for the

(a) physical laboratory test model   (b) shell element based model   (c) solid element based model
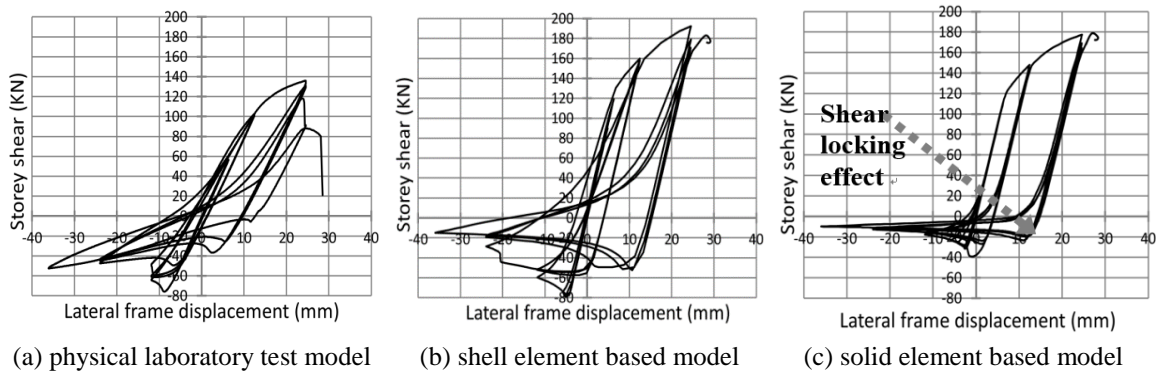
Fig. 6 Plots of base shear versus lateral frame displacement for specimen S60-CA-G1-5

elastic model, a standardised E value equals to 190000 MPa and a Poisson ratio value equals to 0.3 were used in the models. The actual yield strengths were retained from tensile coupon tests (Hunt 2013).

3.2 Element and mesh size

Specimens involved in this study had a periodic buckling and yielding response under fully reversed cyclic axial loading. An element capable of capturing the effects of geometric changes and material degradation was required. In this context, two types of models were developed;

(i) Solid element-based model, which comprises three dimensional cubic solid elements (C3D8R) and

(ii) Shell model, which comprises four node doubly curved elements, designated as S4R.

Beside conventional pros and cons of the two models, the biggest advantage of using the solid model is the possibility of incorporating extended finite element method (XFEM) to its modelling framework. With XFEM, a crack can be modelled independently of the requirement of a dense mesh by methods of partition of unity and cohesive element superimposition. On the other hand, shell element-based models are popular in structural analysis of problems involving bending behaviour such as bending response of brace gusset-plate specimen.

Fig. 6 shows the responses of the two FE models and a physical laboratory test model under cyclic axial loading. As evident, the solid element-based model fails to represent the actual hysteretic response, which is more closely captured by the shell model. Moreover, the solid element-based model consumes modal runtime three times greater than the shell model (13 hours) when simulating an identical model using an Intel core 7 CPU. Also, the solid element-based model had an occupied storage capacity greater than 2.4 times the storage capacity required by the equivalent shell model. The poor performance of the solid element-based model is attributed to several factors, such as the elements (i) are stiff, (ii) lock shear in transverse direction, (iii) possess one integration point, (iv) consume greater model run time and (v) possess less degrees of freedom compared with shell elements.

An element size of $b/22 \times b/22$ was employed at the mid-length of brace, where b is the width of the brace tube. This element size was extended in both directions from the mid-length equal to 1.5 times the dimension of the larger face of the brace section, h, to ensure that the mesh is sufficiently large to accommodate the half wave length of the locally buckled shape, which was
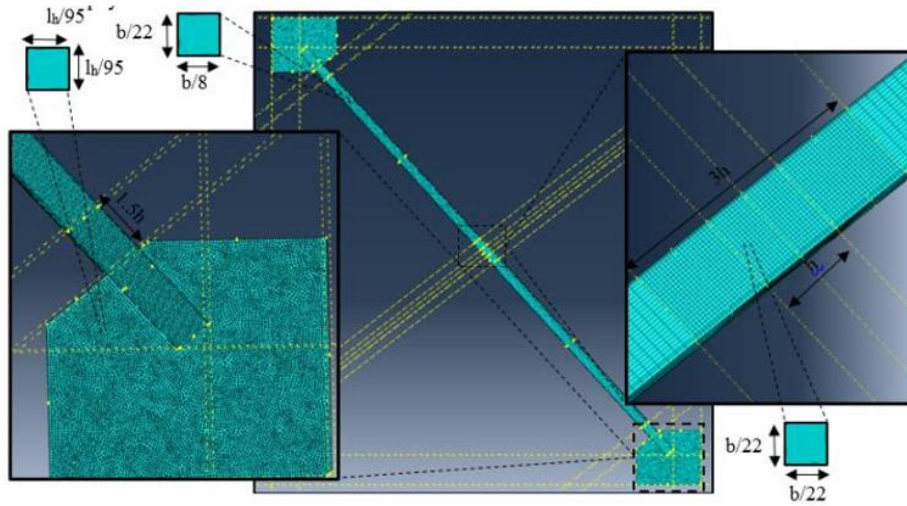
Fig. 7 FE model of S40-CA-G1-1 specimen with mesh detailing in measuring unit (mm)

Table 4 Results of linear buckling analyses and their comparison to physical laboratory test and FE outputs in relation to response of specimen under fully reversed cyclic axial loading

Specimen	k	$\bar{\lambda}$	N_{cr}	F_c/N_{cr}	F_c/N_{cr}	F_c
			(kN)	Test	FE	FE/Test
S40-CA-G1-1	0.68	1.41	-63.08	0.61	0.88	1.44
S40-CA-G2-2	0.84	1.83	-37.39	0.57	0.62	1.09
S40-CB-G1-3	0.72	1.49	-56.76	0.74	0.92	1.24
S40-CB-G2-4	0.85	1.86	-36.13	0.90	0.91	1.00
S60-CA-G1-5	0.86	1.10	-143.89	0.79	0.86	1.09
S60-CA-G2-6	0.94	1.27	-109.66	0.82	0.92	1.12
Mean				0.74	0.85	1.16
Cov				0.16	0.12	0.12

approximately assumed equal to the larger face of the section (Nip *et al*. 2010, Nip *et al*. 2013). The gusset plates at each end of the braces were modelled and meshed with elements of size $l_h/95 \times l_h/95$, where l_h is the width of the gusset plate (Table 2). This mesh size was extended 1.5 times the dimension of the larger face of the brace tube beyond the gusset plate to accommodate the half wavelength of the locally buckled shape in this region. An element size of $b/8 \times b/22$ was used for the uncritical remainder region of the model. This element size ensures that the model has a sufficient number of elements to form continuum sinusoidal waves in regions that are non-critical (Fig. 7).

In tests, the lower gusset plate was fixed to the test frame at the bottom edge only and the upper gusset plate was connected to the frame in accordance with connecting details designed, such as CA and CB (refer to Table 2). Identical boundary conditions are used in FE models to those in the physical tests with fixed constrained end condition.

3.3 Linear buckling analysis

A linear buckling analysis was carried out to determine the global slenderness of specimens. The specimens were provided with identical boundary conditions to that of the physical tests and were then loaded in axial compression. The resulting elastic critical buckling load was estimated corresponding to the second Eigen buckling mode shape. Table 4 contains the results of the linear buckling analysis in terms of global slenderness ratio, $\bar{\lambda}$, defined in Eq. (2), (where A is the brace tube cross-section, f_y is yield strength of brace), effective buckling length factor, k, elastic critical buckling load, N_{cr} and ratios of N_{cr} relative to the initial buckling loads, F_c, obtained from physical tests and FE models of specimens when subjected to cyclic axial loading.

$$\overline{\lambda} = \sqrt{\frac{A\,f_y}{N_{cr}}} \qquad (2)$$

Brace gusset-plate specimens that were detailed as per conventional design have a k value of between 0.68 and 0.86, while specimens that were detailed according to the balanced design methodology have a k value between 0.84-0.94. In conventional design, the use of thicker and larger gusset plate leads to a stiffer connection restricting the buckling wave length of specimen, whereas the thinner and compact gusset plate that resulted from the balanced design approach were closer to an idealised pin connected (that is, towards k = 1.0). Furthermore, braces connected to both beam and column (i.e., type CA) have a smaller k value than those connected to the beam only (Type CB) due to increased stiffness of the gusset plate by connecting to both beam and column (Table 4).

In Table 4, it can be seen that the ratio of elastic critical buckling load (N_{cr}) to buckling load values (F_c) from both the physical tests and FE models are below unity, indicating that geometrical imperfection had influence on the global buckling response of specimen. The lowest ratio was found for test specimen S40-CA-G1-1, which was due to deformations that were observed in the lower channel section connecting the lower portion of the brace to the reaction frame during testing. This channel section was replaced with a strengthened one for later tests. On the other hand, a very good correlation is found between the results obtained from linear buckling analysis and the numerical models with a mean value of 0.85 and coefficient of covariance (C_{ov}) of 0.12. This good agreement is partially due to the geometrical imperfection model employed.

3.4 Geometrical imperfection model

Geometrical imperfections are the largest source of uncertainty in building the numerical model due to their non-uniform distribution that can be difficult to predict and measure. Design codes typically take imperfections into account when determining the buckling capacity of steel members under axial compressive loading. The magnitude of these imperfections are determined based on a number of parameters, such as the cross-sectional shape and size, grade of steel and manufacturing method (see, for example, EC3 (CEN 1993). Design codes, however, do not provide guidelines on the magnitude and distribution of imperfections for building models in a FE framework. Thus, Goggins (2004) intended on contributing to this limited data by proposing a range of measured imperfections for application to simulation of single-story single-bay braced steel frame. In addition, Salawdeh and Goggins (2013) went further by investigating imperfections primarily on steel bracing members. However, the scope of the investigation was confined around half-sine wave shape imperfection along with limited imperfection magnitudes. To overcome this issue, Hassan *et al*. (2018) investigated imperfection from the broader aspect by assessing three of

the most applied methods of imperfection with a broader range of magnitudes of imperfection. Their results showed that FE models gave best predictions of physical tests when they were modelled with a combined equivalent notional lateral load and sinusoidal wave imperfection, where the former imposed a global imperfection with an initial lateral deformation at mid-length of the brace, ω_1, equal to L/1000 and the latter imposed local imperfections whose magnitude, ω_2, was determined by an expression given by Gardner *et al.* (2010) for cold-formed steel

$$\omega_2/t = 0.034 \, (f_y/\sigma_{cr})^{0.5} \tag{3}$$

where t is the plate thickness, f_y is the material yield stress and σ_{cr} is the plate critical buckling stress.

The global imperfection governs the magnitude of the initial buckling capacity of the specimen, while the local imperfection improves the response of the structural element during softening stage. Therefore, the model of Hassan *et al.* (2018) was used in this paper, in which the magnitude of global imperfection, ω_1 was set equal to $L_b/1000$ (to comply with buckling curves in EC3 (CEN 1993), where L_b is brace tube length, while the magnitudes of local imperfections, ω_2 were derived using Eq. (3). To incorporate the imperfection model into the finite element model, a code was written using the programming language python. The code details are given in Hassan *et al.* (2018).

3.5 Finite element solver

ABAQUS (2013) offers various solvers to solve non-linear structural response problems using large deformation theory. Among them, the general-purpose static solver and the low cycle fatigue solver were assessed. A low-cycle fatigue solver solved fatigue issues associated with linear geometric changes, which can be solved with general static solver, including fatigue issues of nonlinear geometric changes. Hence, a general static solver was used with activated non-linear option to stimulate inelastic response of structural steel elements. A tabular format is employed to apply cyclic loading incrementally. The increment size was set at 0.0085mm per cycle with the number of increments varying according to the loading history, but with a maximum number of increments set at 10^6. The maximum number of iterations was set at 20 iterations (default in ABAQUS is 5) to deal with finding solutions during non-linearity behaviour of the system, particularly in the stages of brace buckling and yielding. Buckling and yielding of braces develop plastic hinges at corners of the mid-length brace tube section, which can form cracks upon maturity, leading to a reduced cross-section capacity and ultimate failure.

3.6 Fatigue-life model

As fatigue was not explicitly captured in the models, a predictive model for fatigue was required. A predictive model can be micro-mechanical, meso-scale or macro-scale models. All forms of fatigue model consider appropriate constitutive parameters to justify the scale of damage and the resulting fatigue. However, very limited models address earthquake type fatigue. Of them, the Coffin and Manson model (Manson 1953, Coffin 1954), which is a reflective of the meso-scale damage model and the Kavinda and Deierlein (2004) model, which is reflective of micro-mechanic model, were assessed. It was found that, although, micro-mechanical models assess fatigue very locally, they are complicated to implement into computational plasticity due to their modelling requirement, such as fine mesh, characteristic length feature, etc. In contrast, meso-scale

models operate over coarser to fine meshes, requires less modelling parameters, saving cost and time of post-processing. Therefore, the Coffin and Manson meso-scale model (Manson 1953, Coffin 1954) was used in this study. Another reason of opting for this model is the fatigue quantification with strain magnitudes, which makes the model competent for dealing with fatigue in strain-controlled tests. The model provides the number of reversals to failure for a given plastic strain, as defined by Eq. (4).

$$\frac{\Delta\varepsilon_p}{2} = \varepsilon'_f (2N_f)^C \tag{4}$$

where $\Delta\varepsilon_p/2$ is the plastic strain amplitude, ε'_f is the fatigue ductility coefficient which is the material parameter that roughly indicates the strain amplitude at which one complete cycle on a virgin material will cause failure, C is the fatigue ductility exponent which is the material parameter which describes the sensitivity of the log of the total strain amplitude to the log of the number of cycles to failure and N_f is the numbers of reversals to failure.

These reversals then linearly accumulated into a series of fatigue indexes by mean of a cumulative damage rule, known as Miner's rule (Palmgren 1924), which is defined as

$$DI = \sum_{i=1}^{n} \frac{n_i}{N_{fi}} \tag{5}$$

where N_{fi} is the number of reversals causing failure at a strain level of ε_i and n_i is the number of reversals for which that strain level is applied.

The sum of these fatigue indexes indicates the degree of exclusive fatigue from 0 to 1. At a fatigue index of 1, it is highly likely the fatigue failure has evolved in the specimen at a region where the strain outputs had been extracted and the resulting cycle is marked as fatigue-life cycle.

For fatigue prediction, a fatigue evaluation criterion was required in tests and FE models. For tests, the initiation of a crack in the corner region was marked as fracture occurrences (refer to Table 5). This criterion was used in the FE models to extract strain outputs for fatigue prediction. In FE models, however, it was unclear about the extent of the plastic hinge and the point of integration to be used for fatigue prediction as an accurate mean of assessment. In this context, an assessment methodology outlined by Nip *et al*. (2013) was used. They carried out a detailed study on strain distribution across regions surrounded by plastic hinges, such as brace tube mid-length section. Their study found that an area covering the corner and one-eighth of the buckling wavelength is suitable for fatigue prediction. To predict fatigue, section positive (SPOS) (ABAQUS 2013) point of integration of a shell element can be used for abstracting strain outputs from the FE models as it carries the influence of local buckling, but is less sensitive to mesh size.

4. Modelling validation

Validation of the numerical models under fully reversed cyclic axial loading was carried using measurement data from the physical laboratory tests described in Section 2. Table 5 contains the results of the physical tests in terms of yield tensile load, F_y, ultimate tensile load, F_u, initial buckling load, F_c, energy dissipation capacity, W_{total} and numbers of cycles to global and local buckling including fatigue. These results are obtained by transforming the measured storey shear

Table 5 Summary of test measurements

Specimen	$b/t\varepsilon$	$\bar{\lambda}$	F_y	F_u	F_c	W_{total}	Number of cycles to			
			KN	KN	KN	KN.m	Global buckling	Local buckling	corner opening	fracture
S40-CA-G1-1	16	1.41	118	182.4	-38.4	38.9	3	10	16	17
S40-CA-G2-2*	16	1.83	152	215.7	-21.4	52.2	3	-	28	29
S40-CB-G1-3	16	1.49	175	200.1	-41.9	36.8	3	10	21	23
S40-CB-G2-4	16	1.86	188	209.8	-32.7	61.7	3	10	28	29
S60-CA-G1-5	24	1.10	196	211.7	-113.4	18.8	4	6	10	11
S60-CA-G2-6	24	1.27	190	204.5	-90.1	20.1	4	7	10	11

*survive maximum ductility demand

Table 6 Summary of FE results

Specimen ID	$f_{y,g}$	f_y	Initial geometric imperfection		Ratio of FE to physical test results				Number of cycles to		
	$N/m\,m^2$	$N/m\,m^2$	Global ω_1	Local ω_2 Eq.(3)	F_y	F_u	F_c	W_{total}	Global buckling	Local buckling	Fracture
S40-CA-G1-1	271	351	$L_b/1000$	3.6%t	1.45	1.13	1.44	1.04	2	11	16
S40-CA-G2-2*	311	351	$L_b/1000$	3.8%t	0.99	0.95	1.09	0.87	3	28	29
S40-CB-G1-3	284	351	$L_b/1000$	3.6%t	0.98	1.06	1.24	0.80	3	17	19
S40-CB-G2-4	302	351	$L_b/1000$	3.8%t	0.89	0.94	1.00	0.86	2	23	26
S60-CA-G1-5	279	336	$L_b/1000$	2.2%t	1.30	1.45	1.09	1.49	3	7	9
S60-CA-G2-6	315	336	$L_b/1000$	2.4%t	1.21	1.13	1.12	1.13	2	8	10
Mean					1.14	1.11	1.16	1.03			
Cov					0.18	0.15	0.12	0.23			

*survive maximum ductility demand in test, "t" is brace tube thickness and L_b is brace tube length

force and lateral frame displacement into brace axial force and elongation. For convenience, the actual plots of storey shear force and lateral frame displacement of each specimen are presented in Figs. 8-13. Moreover, Table 6 contains the predictions from the numerical model and corresponding comparisons with physical test measurements. It also contains essential data used in modelling the gusset plates and bracing members.

4.1 Yield strength, initial buckling and post buckling loads

The axial load to initially yield the specimens was approximated using the $1/10^{th}$ slope method. In this method, yield values correspond to the point where the tangent at the origin and the tangent that has a slope of one-tenth the tangent at the origin intersect. From Table 6, while comparing the initial yield load values of FE models to those obtained from physical tests, it was found that FE models gave a good prediction of initial yield loads with the mean being 1.14 and Cov 0.18 for all specimens investigated. On the other hand, the ultimate load, defined as the largest load a
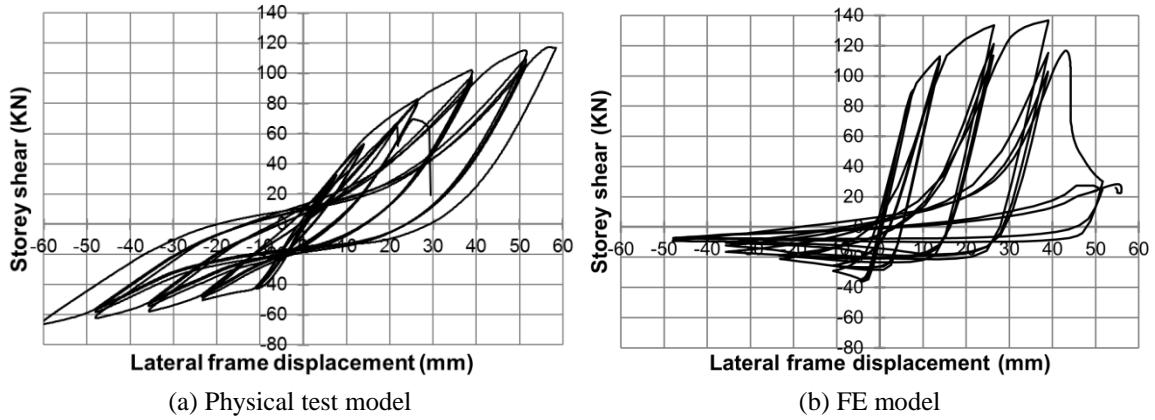
(a) Physical test model   (b) FE model

Fig. 8 Plots of storey shear versus lateral frame displacement of specimen S40-CA-G1-1.

(a) Physical test model   (b) FE model

Fig. 9 Plots of storey shear versus lateral frame displacement of specimen S40-CA-G2-2.

(a) Physical test model   (b) FE model
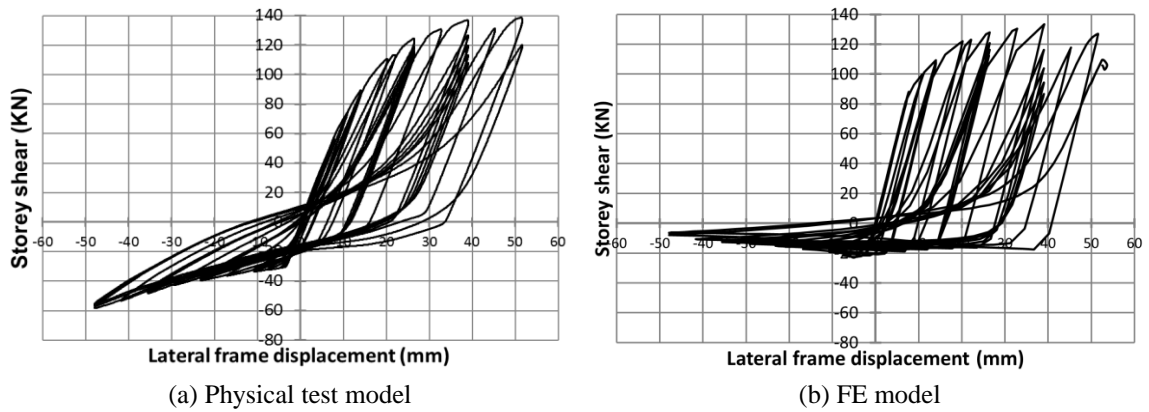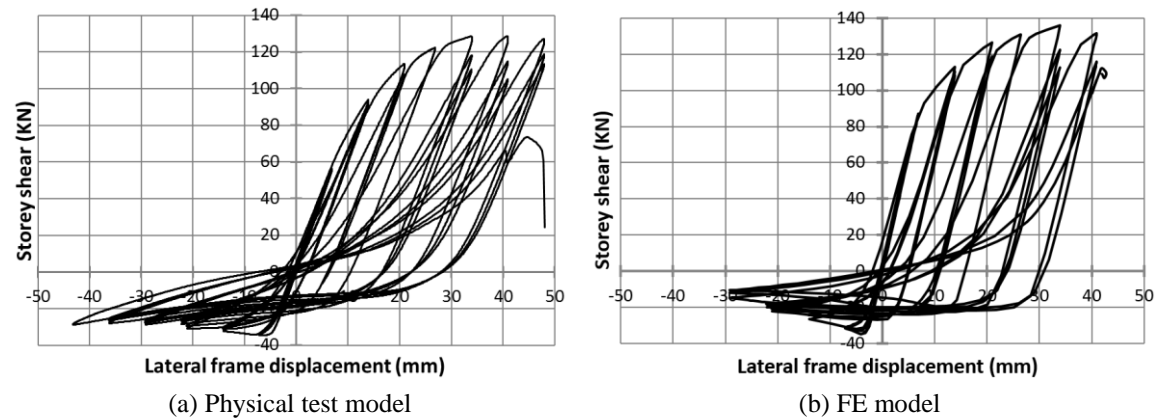
Fig. 10 Plots of storey shear versus lateral frame displacement of specimen S40-CB-G1-3.

specimen carried in tension, was found from the FE models to be on average 1.11 times the physical test results with a Cov on average of 0.15 for all specimens studied.

The initial buckling load (F_c) is typically the highest load a specimen resists in compression. As

(a) Physical test model (b) FE model
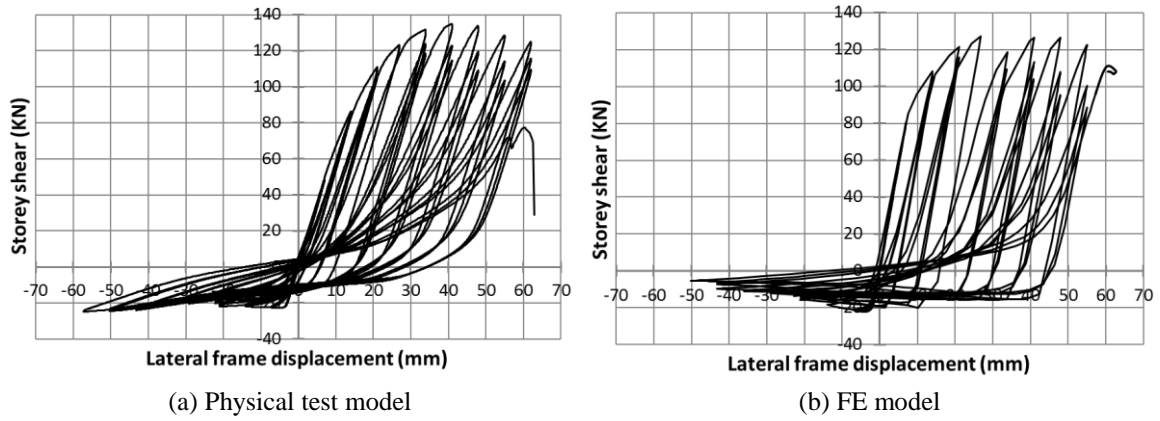
Fig. 11 Plots of storey shear versus lateral frame displacement of specimen S40-CB-G2-4
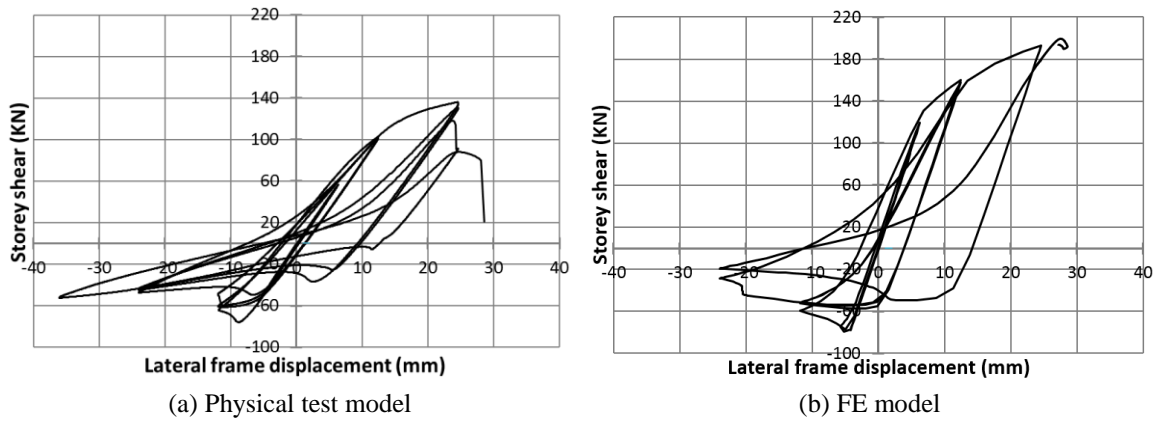
(a) Physical test model (b) FE model

Fig. 12 Plots of storey shear versus lateral frame displacement of specimen S60-CA-G1-5

(a) Physical test model (b) FE model
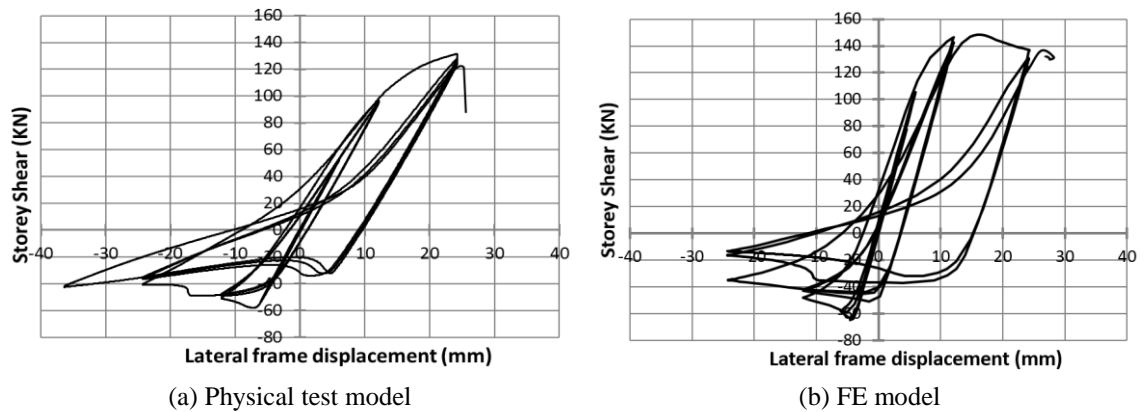
Fig. 13 Plots of storey shear versus lateral frame displacement of specimen S60-CA-G2-6

only Class 1 sections are considered in this study, initial buckling typically occurs in the same cycle in which the specimen yields for stockier members, whereas it happens in earlier cycles for more slender members due to elastic buckling. The results of the physical test model show that
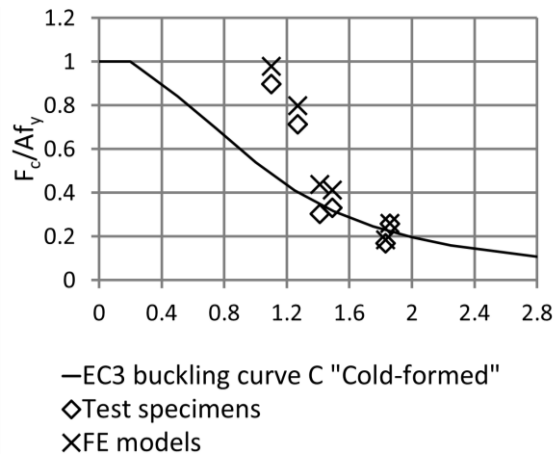
Fig. 14 Plot of normalised initial-buckling loads versus normalised global slenderness ratios for all specimens, including buckling curve from EC3 (CEN 1993)

specimens designed using a balanced design approach carried lower buckling loads than specimens based on conventional design. This difference is attributable to factors influencing gusset plate detailing and slenderness of the bracing members (Salawdeh *et al*. 2017). While comparing FE models to test models, it is found that the FE models gave very good predictions of initial buckling loads, with a mean ratio of 1.16 and Cov of 0.12 for all specimens investigated (Table 6). However, greatest difference arises for the first test specimen S40-CA-G1-1, primarily due to yielding of the supportive channel section during the physical test, which was replaced with a strengthened channel for other tests. FE results show that braces with larger gusset plate connections attain greater buckling load but delivered less ductile response subsequently (refer to Table 6). In contrast, braces with thinner and more compact gusset plates attain lower buckling load, but yield improved ductile response (refer to Table 6). These observations are also evident in the physical test results (refer to Table 5).

Fig. 14 presents the plot of initial buckling loads, F_c normalised by brace yield strength, f_y times brace cross-section, A, against normalised global slenderness obtained in accordance with EC3 (CEN 1993). These buckling loads are compared with the buckling curves given by EC3 (CEN 1993), as

$$\left.\begin{aligned} \chi &= \frac{F_c}{A\,f_y} \\ \chi &= \frac{1}{\phi + \sqrt{\phi^2 - \bar{\lambda}^2}} \text{ but } \chi \leq 1.0 \end{aligned}\right\} \tag{6}$$

where $\varphi = 0.5[1 + \alpha(\bar{\lambda} - 0.2) + \bar{\lambda}^2]$ and F_c is the design buckling load, α is the generalised imperfection factor with a value of 0.49 for cold-formed sections.

As expected, in general, the EC3 (CEN 1993) design buckling curves gave a lower bound (conservative design), although they significantly underestimated the buckling loads obtained from both the physical tests and FE models for specimens with global slenderness ratio between 1.1 and 1.27. This conservatism is due to the generalised imperfection factor to cover various fabrication defects, such as imperfection and residual stresses. In addition, the initial buckling loads of these

slenderness models are close to their yield capacity. This suggests that they had elastic plastic buckling behaviour. The amount of residual stresses and imperfection is typically observed higher in cold-formed sections than hot-rolled sections, primarily due to further post-fabrication process that is cold-working. The larger imperfection factor for cold-formed curves is inferred to this reason.

Tremblay (2002) proposed a model for evaluating of post-buckling load of Class 1 brace specimens subjected to symmetrical loading. Nonlinear regression analysis of the measured post-buckling loads for cold-formed sections resulted in the proposal of the predictive expressions given by Eq. (7); as

$$a + b_1 \overline{\lambda}^{-c} = \frac{F_c}{A\,f_y}$$ (7)

where a, b_1 and c are the model's parameters which vary in value with respect to the ductility of interest.

Goggins (2004) proposed a similar model by using an independent set of data. The data was also associated to the cold-formed Class 1 brace tubes and, generated experimentally through symmetric loading protocol applied to tubular members. Unlike Tremblay, Goggins (2004) used an upper envelope to develop the expression given in Eq. (8)

$$b_1 \overline{\lambda}^{-c} = \frac{F_c}{A\,f_y}$$ (8)

Fig. 15 presents a comparison of the post-buckling loads obtained from FE and tests models, along with predictions of Tremblay (2002) and Goggins (2004). The values of the parameters in the Tremblay model were 2.5 and 3.1 for b_1 parameter, 3.9 and 5.2 for a and 5.9 and 3.5 for c, for ductility 2 and 4, respectively. In the Goggins model, these values were 5.9 and 2.2 for b_1 parameter and 3.6 and 2.9 for c parameter in accordance with ductility 2 and 4, respectively. A post-buckling load relative to the first cycle of the displacement demand was used. As depicted, Tremblay's model consistently underestimates predictions for ductility levels of 2 and 4. In contrast, Goggins' model gave a relatively better prediction for ductility level of 2, although, in general, underestimated the post-buckling capacity at both a ductility of 2 and 4. This is due to number of possible reasons, including, (i) Tremblay (2002) employed a lower bound definition of the post-buckling compressive strength in Eq. (7) and (ii) for identical slenderness range, the models of Tremblay (2002) and Goggins (2004) did not effectively cover the data of the test specimens.

In Fig. 16 (a)-(b) normalised post-buckling loads are plotted against various ductility levels for both physically tested and numerical models. As depicted, post-buckling loading capacities degraded as the demand of axial ductility increases for all specimens, except of S40-CA-G1-1 and S40-CA-G2-2. A possible reason would be the influence of frame action due to the CA type connection employed in tests 1 and 2. In tests 5 and 6, the influence of the CA connection is never fully realised because the higher cross-section slenderness ratio (from the S60 section) is dominant and causes fracture at earlier post buckling cycles. In general, the degradation in strength is the result of hinge formation at brace mid-length tube section. However, degradation in the post-buckling capacity varies with the slenderness ratios. Specimens with larger global slenderness may not suffer identical compressive strength degradation than the specimens with lower global slenderness ratio, provided that the local slenderness is identical.

(a) Ductility 2   (b) Ductility 4
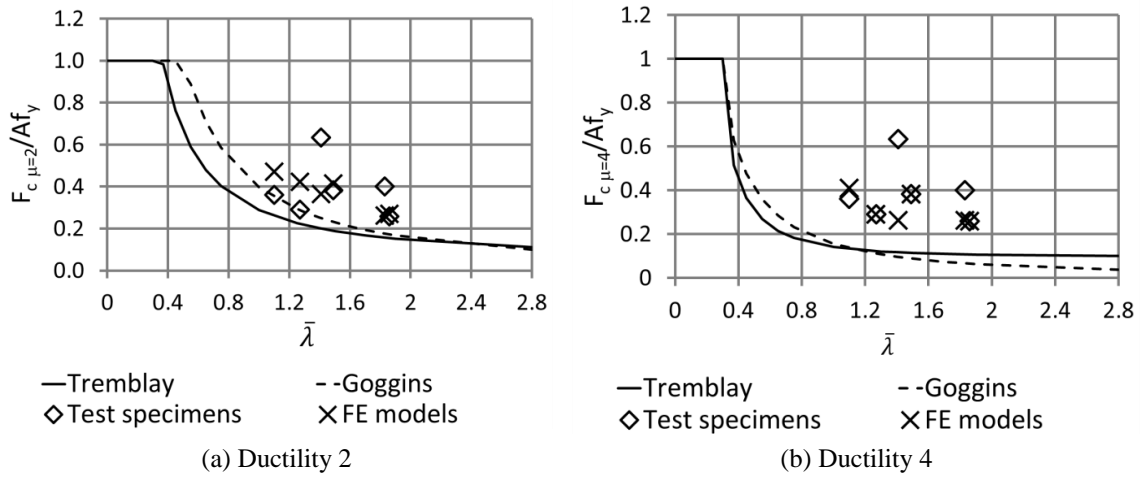
Fig. 15 Plots of normalised post-buckling loads versus normalised slenderness ratio, including predictions from Tremblay (2002) and Goggins (2004)

(a) Physical test models   (b) FE models
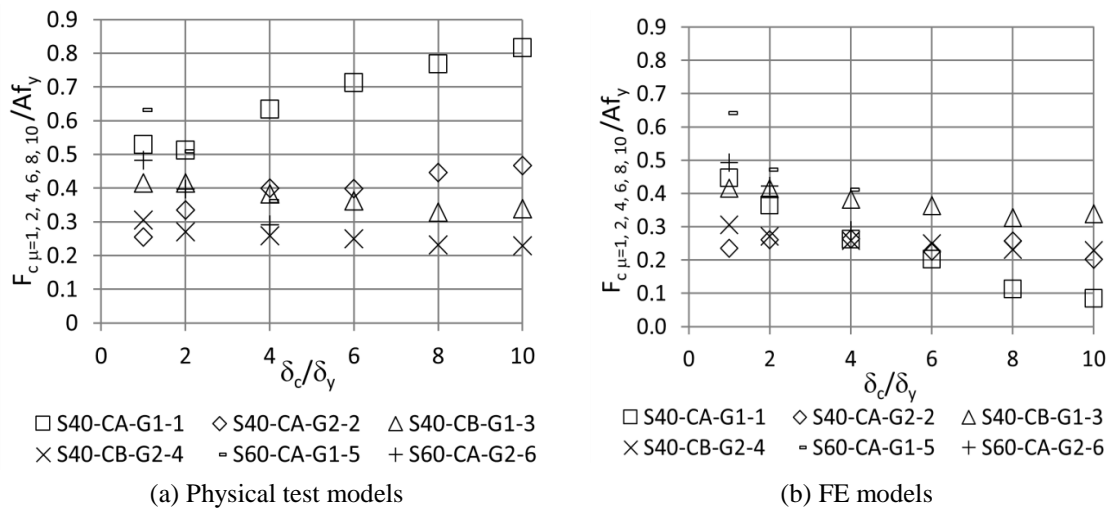
Fig. 16 Post-buckling compressive strength of specimens

While comparing the post-buckling loading capacity of the physical test and FE models, it is found that a good correlation exists between the two models, except for where the frame had unintended deformation in the lower channel section (S40-CA-G1-1).

4.2 Lateral deformation

In the system under consideration, lateral deformation occurs as a result of out-of-plane bending. For design considerations, it is important to be able to predict the deformation of brace members in the normal direction of the loading. For example, it can be used to determine the clearance required between bracing members and non-structural members like glass, cladding, etc for safety purposes. In tests and FE simulations, all models deformed in the out-of-the-plane

direction. However, in the absence of measured data, the results of the lateral deformation from the FE models are only presented.

Tremblay (2002) proposed a simple model for determining lateral displacements as a function of applied displacement, δ_c and brace tube length, L_b, as

$$\Delta = 0.7\sqrt{\delta_c\, L_b} \tag{9}$$

where Δ is the lateral deformation, δ_c is the applied displacement, L_b is the brace tube length and 0.7 is a factor that represents all end conditions implicitly.

Hassan *et al*. (2015) modified the model proposed by Tremblay by incorporating an imperfection factor. A least square regression analysis of the analytical data resulted in the proposal of the predictive expression given by Eq. (10).

$$\Delta = \Gamma.\frac{\omega_1}{L_b}.0.7\sqrt{\delta_c\, L_b} \tag{10}$$

$$\Gamma = \frac{0.97}{\beta^{0.96}} \tag{11}$$

where Γ is a model parameter and should be obtained from Eq. (11). In Eq. (11), β is the ratio of global imperfection magnitude, ω_1 and brace tube length, L_b. Eq. (10) is valid for global imperfection magnitudes ranging from L_b /5 to L_b /2000.

Fig. 17 presents results of the FE models and those obtained from Eqs. (9) and (10). The FE results correspond to the models of Standard Linear Clearance method are shown collectively in Fig. 17(a). In Fig. 17(b), FE results corresponds to Elliptical Clearance method are plotted. As depicted, the model of Hassan *et al*. (2015) gave a very good prediction of lateral deformations. In contrast, the model of Tremblay (2002) overestimates FE predictions significantly, primarily due to the fact that model yields lateral displacement relative to the mechanisms formed by the plastic hinges at ultimate load level.

4.3 Number of cycles to global buckling and local buckling

The instant of global buckling is typically defined by the largest load attained in compression. The identification of the cycle during which buckling occurs is easy identifiable for sections having intermediate to lower slenderness ratios, as these sections have pronounced global buckling following local buckling and hinge formation. It is often difficult to identify the onset of global buckling of specimens with larger global slenderness ratios due to their uniform compressive response. For these specimens, care is required when identifying global buckling loads.

From Table 5, it is found that slender specimens experienced global buckling in the 3rd cycle of loading (i.e., with amplitude of $0.75\delta_y$, where δ_y is the expected yield displacement), except for specimens S60-CA-G1-5 and S60-CA-G2-6. These specimens experienced global buckling in the 4th cycle of loading, which is a yield cycle. It is also found that the FE models gave a reasonable prediction of the instance of global buckling when compared to observations from the physical tests (Table 6).

The instant of local buckling can be quantified by two methods from strain readings; (i) by examining strains in the longitudinal direction and (ii) by examining strain rate outputs. In the former method, the magnitude of strains in the longitudinal direction are used to identify the

(a) G1 type gusset plate (b) G2 type gusset plate
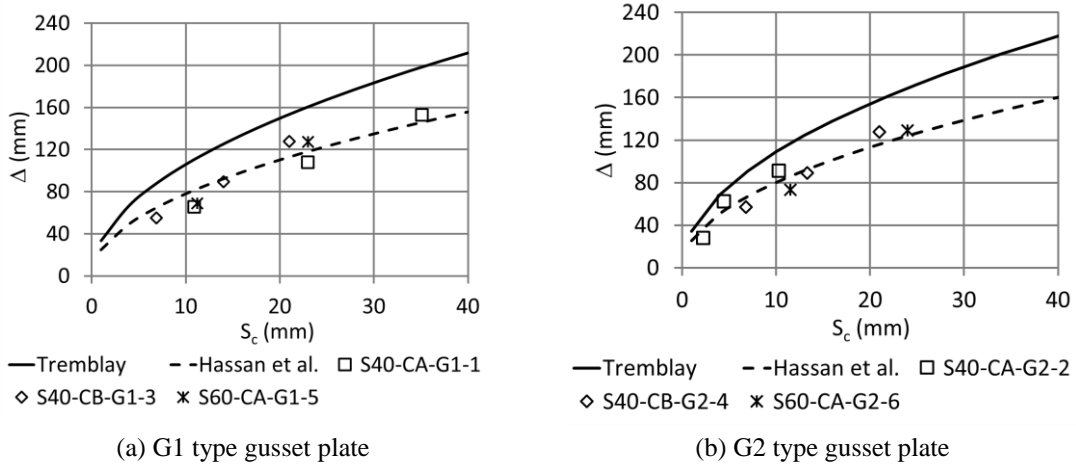
Fig. 17 Plots of lateral deformation of braces against axial displacement magnitude for FE models in conjunction with plots of Tremblay (2002) and Hassan *et al*. (2015).
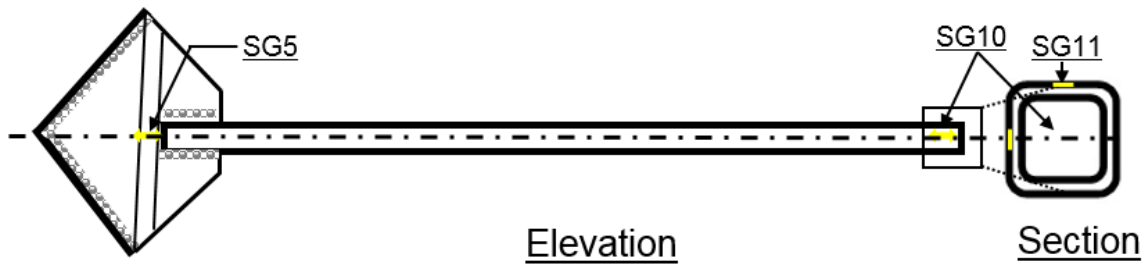
Fig. 18 Location and direction of strain gauges used in the experiments

instant of local buckling. In the latter method the instant of local buckling is indicated by the time when the highest strain rate occurs.

Strain gauges applied to the centre of the outer faces of the specimen at mid-length in the longitudinal direction, identified as SG10 and SG11 in Fig. 18, were used to quantify the instant of local buckling in physical tests. As depicted in Fig. 19(a), SG10 and SG11 have approximately identical strains before the occurrences of local buckling in compression. However, at the instant of local buckling, SG10 displays relatively higher compressive strain readings, primarily due to being located on the outside face of the tube. In subsequent cycles, there is a shift in recordings of SG10 and SG11 from compressive to tensile. This shift is believed to be because local buckling occurs slightly away from the mid-length brace tube section and that the tensile strain is the result of formation of convex rise next to concave slope formed by the local buckling.

Thus, it may not be reliable to use strain gauge recordings in physical tests for quantification of local buckling. To overcome this issue, recordings of strain gauges and loading histories were investigated together (Fig. 19). A sudden change in the loading rate, identified by a sharp narrowness in the load-time plot, can be seen in the compression cycle of the loading when local buckling occurs in test specimen. The presence of this pinching in the time-varying loading plot from the test data is consistent with that observed in the FE models (Fig. 20). It can be concluded that local buckling occurs near mid-length of the brace tube section. However, as stain gauges are

(a) S60-CA-G1-5   (b) S60-CA-G2-6
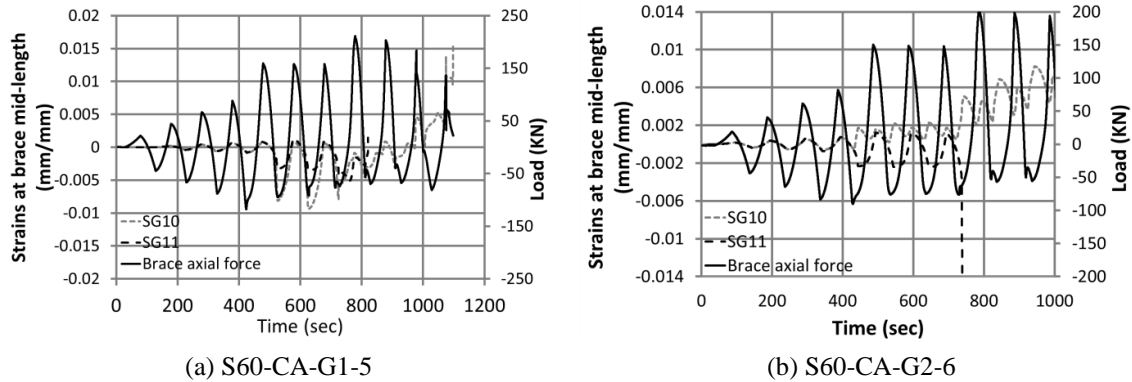
Fig. 19 Plots of measured time-varying longitudinal strains and brace axial force for physical test specimens

placed in discrete points that didn't necessarily coincide with where local buckling was present, restricted the exact identification of the cycles causing local buckling in physical tests. For future experiments, real-time digital image correlation (DIC) offers the potential to overcome this issue.

On the other hand, Fig. 19(b) shows a completely different picture of recordings of the two strain gauges for specimen S60-CA-G2-6. Such that, the strain values from SG10 and SG11 deviated from each other following the occurrence of global buckling. This effect is due to the occurrence of global buckling in the negative direction in relation to the location of SG10 strain gauge. As a result, SG10 records positive (tensile) strains for the entire loading history. This SG10 recording indicates that specimen never regained its original position after experiencing inelastic global buckling in compression. On the other hand, recording of SG11 shows that it has identical pattern of the strain gauge recording obtained on SG11 of specimen S60-CA-G1-5 (Fig. 19(a)). However, it fails in compression as a result of concave deformation next to convex rise formed by local buckling of the upper face at mid-length of the brace tube section.

Fig. 20 presents time-varying lateral strain, strain rate and brace axial forces plots for two FE models identified as (a)-(b) S60-CA-G1-5 and (c)-(d) S60-CA-G2-6. These strain recordings were abstracted from shell elements located at mid-length and mid-section of the braces. As seen in Fig. 20, the compressive strain rate is the largest at the instance where there is a sudden change in the unloading rate during the compression cycle of the loading, resulting in a sharp narrowness in the load-time plot, which indicates that local buckling has occurred at this instance in the FE models.

Thus, observing the loading rate can successfully be used to identify the instance that local buckling first occurs, as well as identifying the instant of global buckling. Furthermore, a shell element has at least three integration points, in which one point records stress/strain history of the outer integration point, while another records histories for the inner integration point. The outer integration point experienced relatively larger compressive strains than inner integration point, due to local buckling.

From Table 5, it is found that all test specimens buckled locally in the second and fourth ductility level, except for the specimen identified as S40-CA-G2-2. The visual inspection of this test specimen had indicated presence of limited local buckling (Hunt 2013). It was, however, difficult to quantify the intensity of this limited local buckling because; (i) it had buckling in the negative direction making it difficult to locate local buckling using available strain gauge measurements (SG10), (ii) the working range of strain gauges was limited, (iii) the response of
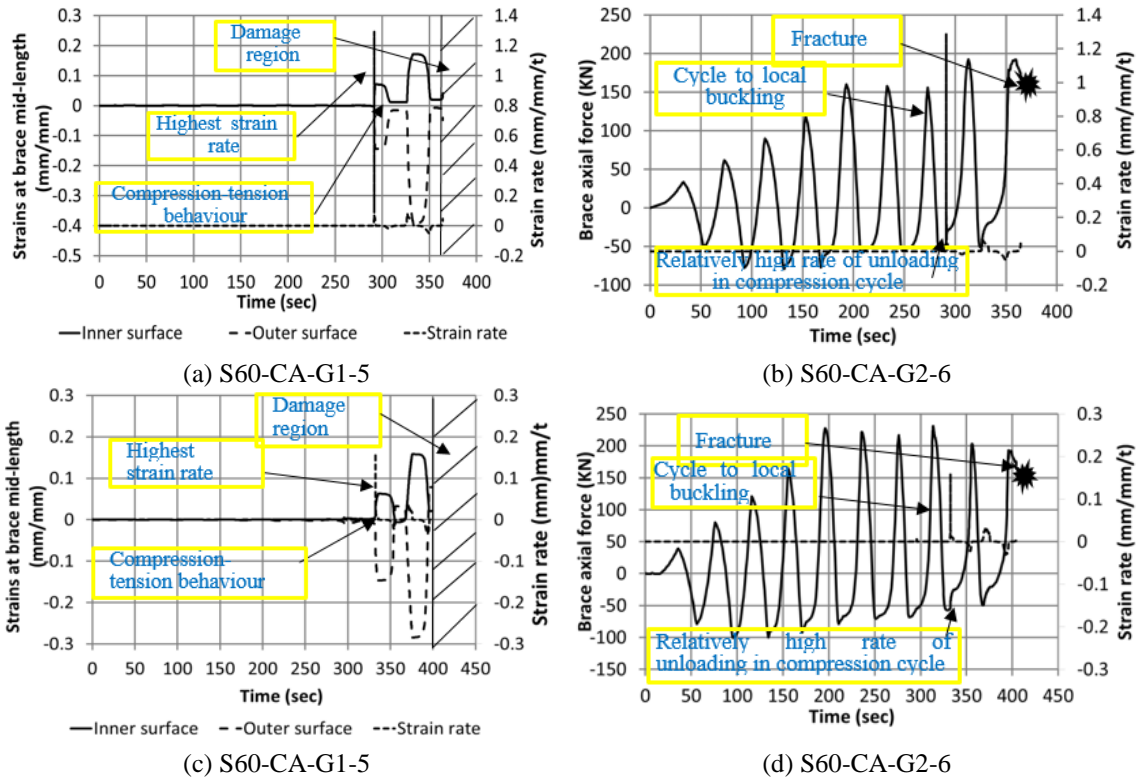
Fig. 20 Plots of (a-b) time-varying longitudinal strain (primary) and strain rate (secondary) from FE models and (c-d) plots of time-varying brace axial force (primary) and strain rate (secondary) from FE models

specimen was highly uniform in bending, making difficult to locate local buckling using loading history and (iv) the specimen survived maximum ductility without failure meaning it is highly likely the failure mode of specimen is global buckling.

As expected, the occurrences of the local buckling significantly degraded the compressive strength of specimens under axial cyclic loading. However, physical tested specimens lasted between 4 and 19 cycles after local buckling before fracture (Table 5), whereas the FE models predicted fracture after 1 to 5 additional cycles after local buckling (Table 6). The specimens are classified as Class 1 sections according to EC3(CEN 1993), which means those tubes have a tendency to form plastic hinges with the rotation capacity without reduction of the resistance before yielding. EC8 (CEN 2004) implies that Class 1 cross-section tubes should be utilised when a high dissipative structural response is desired, whereas Class 2 and Class 3 sections can be used when a low dissipative structural response is suitable. For these sections, local buckling is the limit state to quantify the member capacity. In such cases, quantification of the local buckling becomes important crucially in the CBF design.

4.4 System behaviour

A crucial criterion for accurate prediction of fracture is reproducing the strain distribution correctly in the FE models. The FE and physical test strain measurements over the loading history

of specimen S40-CA-G1-1 and S40-CA-G2-2 are compared and presented in Figs. 21 and 22, respectively. The FE strain output was extracted from similar locations as the strain gauges (Fig. 18). As shown, FE models acceptably reproduced strains measured in the physical tests. The few discrepancies are (i) due strains in the physical tests exceeding the working range of the strain gauges and (ii) may be attributed to the framing imperfection that may arise during testing set-up and experimentation.

While investigating strain recordings of SG5, it is found that the gusset plate of specimen S40-CA-G1-1 remained elastic throughout the loading, while the strains in the gusset plate of specimen S40-CA-G2-2 exceeded the elastic range (Figs. 21-22). This difference is primarily dedicated to the design philosophies and that the balanced design approach used in designing S40-CA-G2-2 allows plastic yielding and, thus, tends to contribute to the system ductility. In contrast, no such yielding is permitted in conventional design, which was used for specimen S40-CA-G1-1.

To examine the component behaviour of a system, similar strain recordings are used. In Fig. 21, specimen S40-CA-G1-1 experienced positive tensile strain at the gusset plate, while it experienced negative compressive strain over the front and top surfaces of the mid-length brace tube section when the time is 1000 sec. A gusset plate tends to bend in the opposite direction relative to the buckling mode of steel braces to accommodate brace end rotation at the connected ends. This is the reason behind the positive (tensile) strain in the gusset plate. The negative strain recording at the brace tube mid-length is the result of formation of the local buckling; however, the formation of convex rise as a result of concave slope tends to shift the behaviour of the strain gauge recording from compressive to tensile.

Fig. 22 shows a completely different picture in the strain gauge recordings of S40-CA-G2-2 specimen compared to those found in tests of S40-CA-G1-1 specimen. The specimen S40-CA-G2-2 was buckled in the negative direction out-of-the-plane of the testing frame. As a result, SG10 records tensile deformation in the opposite face of the locally buckled brace tube. The strain recording of the SG11 shows no effect of this negative buckling and it has identical pattern of the strain recording obtained in specimen S40-CA-G1-1 (Fig. 21(a)). The strain gauge recording SG5 of the gusset plate shows positive (tensile) strains, primarily due to bi-axial inelastic plate buckling in the opposite direction.

4.5 Fatigue prediction

On the basis of cross-section classification, the design limit of the specimens was found to be fatigue-life. A crack usually occurred at mid-length of the brace a few cycles after the first onset of local buckling. Phenomenologically, the occurrence of local buckling develops high compressive strains at upper and lower corners of the brace tube section at mid-length and that upon load reversal transform into tensile stresses, leading to corner opening of the brace tube at mid-length. The stress transformation from compressive to tensile is not purely axial; there is highly likely that a complex tri-axial stress phenomenon occurs causing the formation of plastic hinges. This is the fatigue phenomenon when the scale of assessment is macroscopic or mesoscopic. Micromechanically, a fatigue is the result of micro-cycling degradation process of a material matrix (Rudland and Brust 1997). In the case of braces, material matrix could be assumed to be the region surrounding the plastic hinges as it is where the crack first emerges in tension. Rudland and Brust (1997) found that the micro-cycling degradation process has two important phenomenon (i) crack tip sharpening and (ii) void sharpening. A crack tip sharpened in the compression period of the loading, which upon load reversal caused a micro-crack to join the main crack produced in

(a) gusset plate   (b) brace tube mid-length front face   (c) brace tube mid-length top face
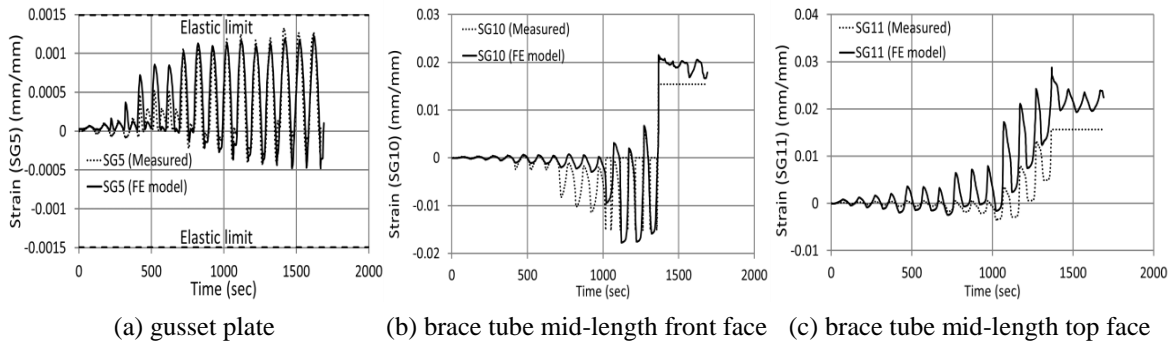
Fig. 21 Plots of strain recording versus time magnitude obtained from FE and test models for specimen of S40-CA-G1-1 at various locations, as identified in Fig. 18

(a) gusset plate   (b) brace tube mid-length front face   (c) brace tube mid-length top face
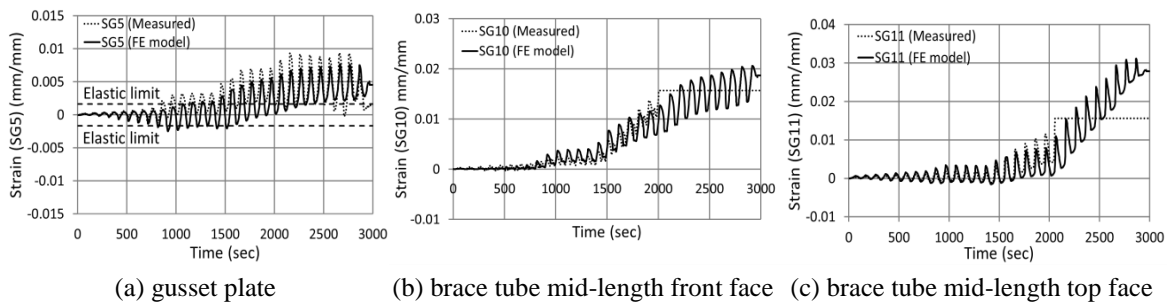
Fig. 22 Plots of strain recording versus time magnitude obtained from FE and test models for specimen of S40-CA-G2-2 at various locations, as identified in Fig. 18

previous tension period to the void ahead of the crack. Crack-tip sharpening was found to be a crucial factor in the evolution of fatigue crack growth, specifically, for symmetric loading.

In Table 5, the number of cycles of loading to fracture due to fatigue is given. On the other hand, fatigue predictions from the FE models are presented in Table 6. A good agreement is found between the two models. The models with lower normalised global slenderness survive a lower number of cycles compared to models with higher global slenderness, which can sustain up to thirty cycles. This difference is due to the central role of the local buckling, which develops earlier in specimens that have lower global slenderness. Moreover, the specimens with balanced design attain a greater number of fatigue cycles irrespective of the connection details. Thus, it can be concluded that a balanced design improves fatigue lives of the bracing members by incorporating gusset plate yielding.

4.6 Ultimate ductility and energy dissipation capacity

A key input into traditional seismic design approaches is a ductility parameter associated with the framing system based on the expected performance of the bracing members. Accordingly, when the response of bracing members is limited to the elastic range, the ductility class is classified as low (CEN 2004). In contrast, if the response is highly ductile (up to plastic hinge formation, which is Class 1 cross-sections in EC3 (CEN 1993)), the ductility class is classified as medium to high (CEN 2004); further stringent guidelines follow for high dissipative structural

response. The bracing members involved in this study are classified as Class 1 cross-section according to EC3 (CEN 1993). Consequently, brace ductility values, μ, are determined relative to the maximum brace elongation at failure, δ, normalised by the axial elongation of the brace at yield, δ_y. This change may be an increase in length (elongation under tension) or a reduction in length (shortening under compression) and includes the effects of axial deformations in the brace tube length and gusset plate strains. The brace yield displacement, δ_y, is obtained as the product of the length of the unstiffened brace tube (actual length – 2 times weld length, where weld length is 100mm) and its characteristic yield strain ($\varepsilon_y = f_y/E$), where f_y is the brace yield strength (Table 6) and E is the modulus of elasticity assumed as 190,000 N/mm^2. The observed values of μ vary from below 6 to above 15, as illustrated in Fig. 23.

Design guidelines do not provide guidance on obtaining ductility capacities of the dissipative elements. However, Tremblay (2002) proposed a simple model, in which the total ductility reached at fracture, μ_T, is related only to the normalised slenderness parameter, $\bar{\lambda}$, as

Cold-formed carbon steel

$$\mu_T = 2.4 + 8.3\bar{\lambda} \tag{13}$$

On the other hand, Goggins *et al.* (2006) working independently on test data, proposed a characterisation of ductility capacity, μ (the change in brace length, δ, at failure normalised by the brace yield displacement, δ_y) based on the normalised slenderness parameters, $\bar{\lambda}$ and width to thickness ratio (b/t) as,

Cold-formed carbon steel

$$\mu = -0.68 + 26.2\bar{\lambda} \tag{14}$$

$$\mu = 29.1 - 1.07(b/t) \tag{15}$$

Nip *et al.* (2010), using similar definition of ductility capacity used by Goggins *et al.* (2006), developed improved expressions for three steel materials, as

Hot-rolled carbon steel

$$\mu = 3.69 + 6.97\bar{\lambda} - 0.05(b/t\varepsilon) - 0.19(\bar{\lambda})(b/t\varepsilon) \tag{16}$$

Cold-formed carbon steel

$$\mu = 6.45 + 2.28\bar{\lambda} - 0.11(b/t\varepsilon) - 0.06(\bar{\lambda})(b/t\varepsilon) \tag{17}$$

Cold-formed stainless steel

$$\mu = -3.42 + 19.86\bar{\lambda} + 0.21(b/t\varepsilon) - 0.64(\bar{\lambda})(b/t\varepsilon) \tag{18}$$

Table 7 compares the peak displacement ductility demand observed in each test in which brace fracture occurred to the ductility capacities calculated using the equations proposed by Tremblay (2002) and Nip *et al* (2010). The peak ductility demand observed in each cyclic test exceeded the ductility capacity, μ, calculated using Eq. (17) in all cases, with the experimental ductility demands ranging from 31% to 122% of the predicted capacity values. On the other hand, the application of Eq. (13) results in predictions of ductility capacity, μ_T, that generally underestimate the peak ductility demand observed prior to brace fracture. Specifically, the experimental ductility

Table 7 Measured and predicted ductility capacities

Specimen	δ_y (mm)	δ_{Test} (mm)	δ_{FE} (mm)	$\mu=\delta_{test}/\sigma_y$	$\mu=\delta_{FE}/\sigma_y$	μ Eq. (17)	μ_T (Test)	μ_T (FE)	μ_T Eq. (17)	$\delta_{FE}/\delta_{test}$
S40-CA-G1-1	4.0	58.4	51.2	14.6	12.8	6.6	30.0	25.0	14.1	0.9
S40-CA-G2-2	4.3	51.3	50.4	12.0	11.8	7.1	23.3	23.3	17.6	1.0
S40-CB-G1-3	4.0	48.1	41.0	12.0	10.2	6.7	22.5	17.5	14.8	0.9
S40-CB-G2-4	4.3	63.0	60.1	14.8	14.1	7.1	27.9	22.6	17.8	1.0
S60-CA-G1-5	3.8	28.6	24.5	7.5	6.4	4.7	12.4	12.4	11.5	0.9
S60-CA-G2-6	4.0	25.6	24.1	6.4	6.0	4.9	12.3	12.3	12.9	0.9
Mean										0.91
Cov										0.06
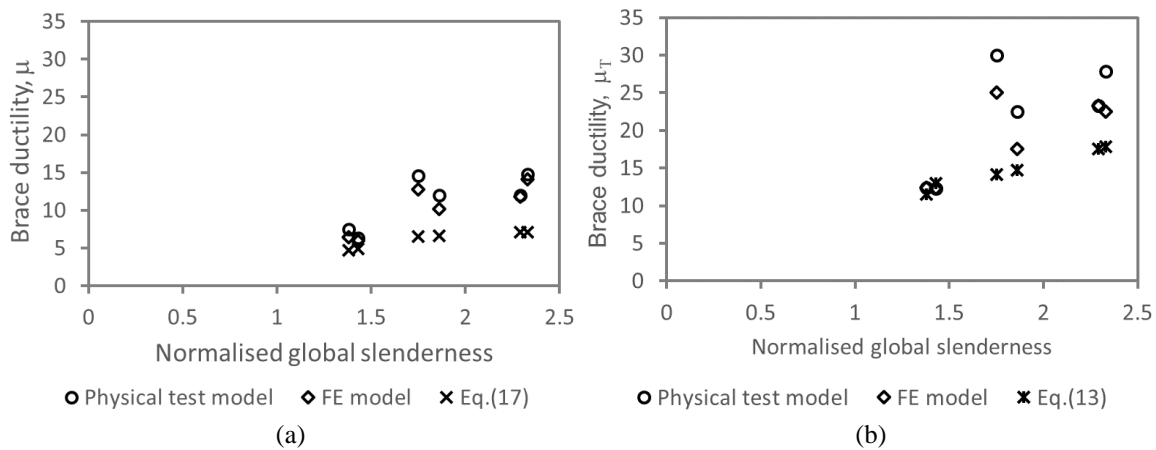
Fig. 23 Comparison of observed peak displacement ductility demand in test to predicted brace ductility capacity in FE models, along with predictions of (a) Nip *et al.* (2010) and (b) Tremblay (2002). Note $\mu=\delta/\delta_y$ for Nip *et al.* (2010) and $\mu_T =(\delta_{elong}+\delta_{shor})/\delta_y$ for Tremblay (2002)

demand in the failure test was greater than the value predicted by Eq. (13) for experiments with brace specimens of 40x40x2.5mm, with the predictions ranging between -32% and -112% of the experimental value.

These data are illustrated in Fig. 23, which indicates that Eq. (17) gave mostly conservative predictions of brace ductility capacity. This conservatism may be due to the limited test data that were used to develop the expression. In contrast, Fig. 23(b) indicates that Eq. (13) significantly over predicts brace ductility capacity for specimens with 40x40x2.5mm tubes. This is likely due to scattering of the data used to develop that expression.

EC8 (CEN 2004) allows concentric steel braces up to global slenderness, $\bar{\lambda}$ between 1.3 to 2.0 and EC3 (CEN 1993) allows cross-section with limiting width to thickness (b/t) ratio less than and equals to 72ε for Class 1 braces subjected to web bending, where $\varepsilon=\sqrt{235/f_y}$, f_y is the nominal yield strength, which is 275MPa herein. Thus, considering these limits imposed by EC8 (CEN 2004), it is possible to use Eqs. (13) and (17) to determine a range of allowable peak displacement ductility for design conveniences. With the maximum allowable global slenderness and the maximum allowable local slenderness, Nip *et al.* (2010) gave an absolute ductility of 6, while it is
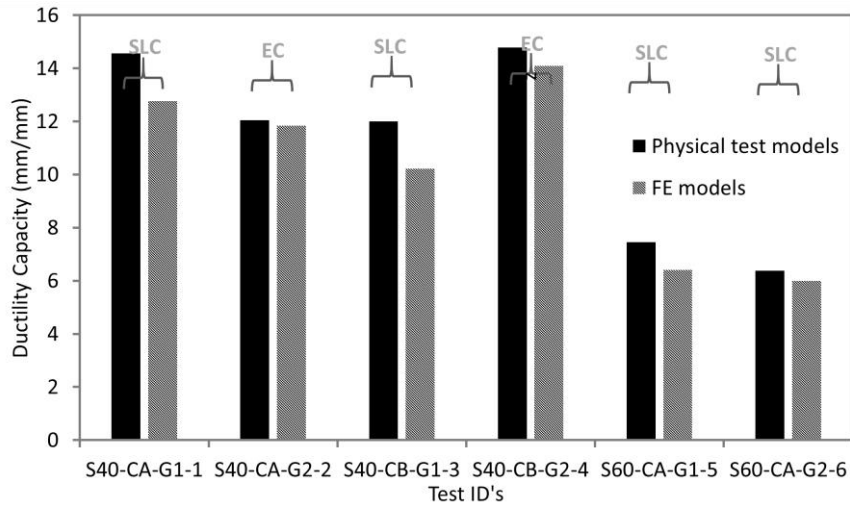
Fig. 24 Ductility capacity of the physical test models and FE models
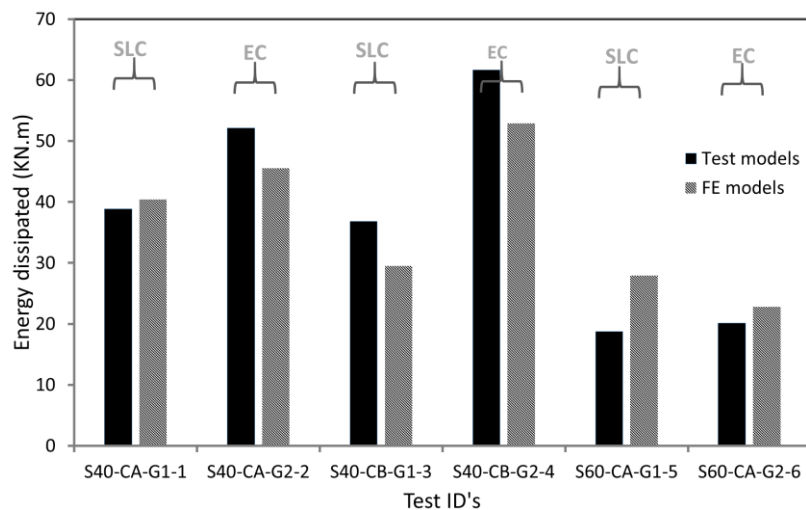
Fig. 25 Energy dissipation capacity of the physical test models and FE models

4 when the minimum allowable global slenderness ($\bar{\lambda}$ =1.3) was used with a constant magnitude of maximum allowable local slenderness. On the other hand, these values were 13 and 19 using Tremblay's model (Tremblay 2002) for the minimum and maximum allowable slenderness (global), respectively.

Fig. 24 compares peak displacement ductility observed in the FE and physical test models. It is found that the FE model gave a good prediction of the measured ductility capacity with a mean of 0.91 and Cov of 0.06.

Energy dissipation capacity is another important measure of structural capacity from the seismic design aspect. It can be defined as an area enclosed by the hysteresis loop under axial compression and tension loading. The effect of the energy dissipation capacity is implicitly accounted in the behaviour q factor in EC8 (CEN 2004) to transform the elastic response spectrum

(a) Occurrence of local buckling at brace tube mid-length (at compressive period 6th)

(b) Corner opening and fatigue occurrences (at tensile period 10th)

(c) Broken brace tube from mid-length (after test)

(d) Gusset plate bent shape after test (after test)
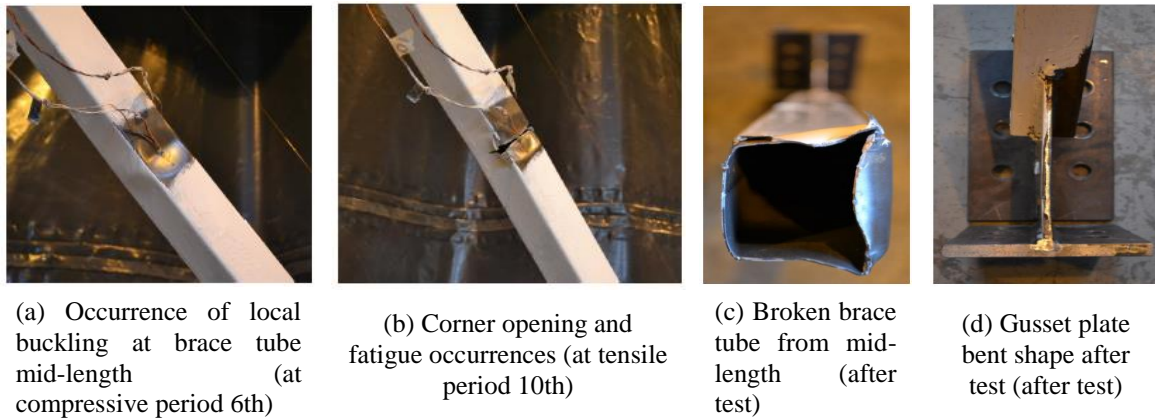
Fig. 26 Snapshots of specimen S60-CA-G1-5 during testing programme

(a) Occurrence of local buckling (at compressive period 7th)

(b) Formation of plastic hinges at upper and lower compressive corners (at tensile period 9th)

(c) Damage occurrence (after simulation)

(d) Gusset plate bent shape after test (after simulation)
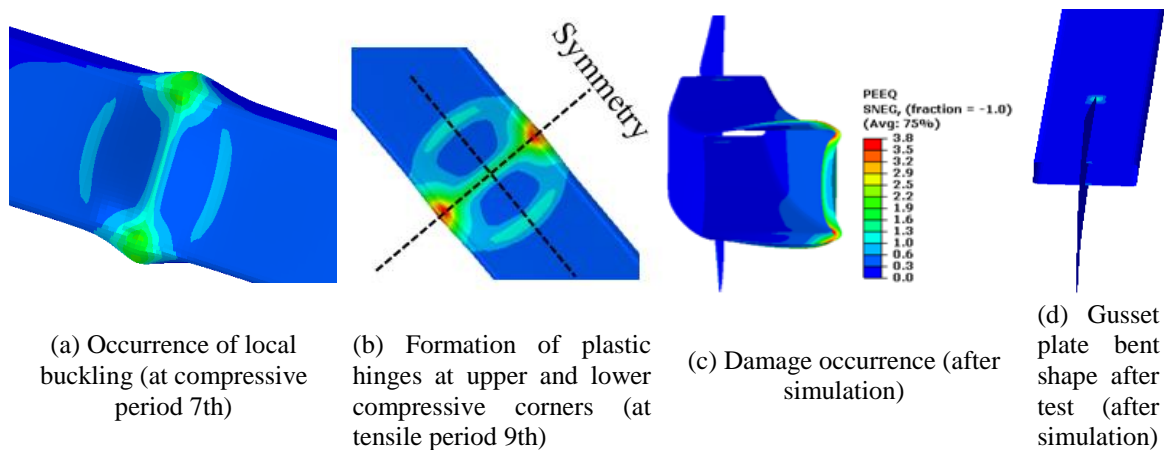
Fig. 27 Snapshots of FE model S60-CA-G1-5 during and after simulation

into a design spectrum to avoid the need to conduct non-linear structural analysis. Fig. 25 presents a comparison of the energy dissipation capacity between physical test and FE models. While comparing predicted to test results, it is found that the FE model gave a close prediction of the brace energy dissipation capacity. Thus, it can be concluded that the FE model provides a reasonable prediction of the test results, validating the accuracy of the model.

4.7 Failure modes

As an example, Fig. 26 shows the experimentally obtained deformed structural behaviour of specimen S60-CA-G1-5 under fully reversed cyclic axial loading. Occurrence of local buckling forms plastic hinges at upper and lower compressive corners, which triggers cracking at these locations and evolve a fatigue upon maturity. In physical experiments, however, without the use of advanced monitoring equipment such as digital image correlation, it is difficult to inspect in detail the life-cycle degradation process of material from initial loading to damage unless analysing it through finite element modelling. Fig. 27 shows the deformed specimen and Von Mises stresses

for the FE model of the specimen displayed in Fig. 26. It can be observed that substantial inelastic deformation occurred by local buckling, followed by formation of plastic hinges and finally damage evolution in the corner regions, which is the typical ductile steel behaviour of cold-formed structural steel square and rectangular hollow sections to failure. This generally follows the visual development of local buckling in the experimental results.

5. Conclusions

The inelastic cyclic response of gusset plates and bracing members in CBFs is asymmetrical and complex with periodic cyclic buckling and yielding, leading to hinge formation and fatigue. These response features are difficult to predict under dynamic loading conditions. Previous research and design guidelines that established the influence of brace slenderness (global and local) on system ductility and energy dissipation capacity was principally based on the testing of steel braces. Design codes are unable to provide clear guidelines on detailing of gusset plate connection primarily due to lack of sufficient data on the response of gusset plates and bracing members with practical structural details and loading conditions. Moreover, finite element models for simulating the cyclic response of braced frames have not always been fully validated due to lack of sufficient data on tests of full-scale models with realistic detailing of brace gusset-plate specimens in a plane CBF structure.

To provide this essential data on the response of CBFs with practical end details and realistic gusset plates, the results of six full scale tests on a plane CBF structure have been examined. Physical measurements and observations from tests made an important contribution by allowing straight forward assessment of gusset plate details, including assessment of comparative base shear against lateral frame displacement and examination of bracing members' fatigue lives under fully reversed cyclic axial loading. The test specimens and testing set-up were more realistic than most of the previous tests published in the literature, which are mainly either static monotonic tests or in other cases, quasi-static tests on steel braces with idealised stiffened connection end conditions.

The CBF frame was subjected to uniaxial loading in accordance with loading protocol recommended for the testing of structural steel specimens exposed to fatigue. The symmetric loading regime employed in the tests simulates braces with identical levels of expected peak deformation demand in tension and compression. The brace-gusset plate test specimens consistently displayed alternating buckling and yielding producing hysteresis loops at culminating in fatigue at brace tube mid length. The recorded responses of gusset plate and steel braces were consistent with those that have been recorded in quasi-static cyclic testing of steel braces. Particularly, the final failure was confined to the thin-walled tubular section themselves, even in tests with yielding of the gusset plate, validating conventional and balanced design methods used to dimension and detail the gusset plates connecting the steel braces with the beams and columns of the CBF. Gusset plate failure was not observed, despite allowing slightly higher proportional yielding in one test specimen. Moreover, the balance factors of the test specimens made an important contribution by examining new threshold limit values for the conventional and balanced design approaches. These threshold limits ranged between 0.38 and 0.52 for conventional design and between 0.75 and 1.03 for balanced design. However, further testing is recommended to investigate the transition between these two design limit ranges.

A finite element modelling developed to predict cyclic response effects in the inelastic response of CBFs has been presented comprehensively in this paper. The finite element models employed in

this study made an important contribution by allowing clear and direct access to salient response features of brace gusset-plate specimens, direct comparative assessment of real time strain measurements and observation of life-cycle degradation process under fully reversed cyclic axial loading. Complimentary analysis and assumptions suitable for CBF design were made to quantify the complexity associated with the geometry of steel braces and gusset plates. A linear buckling analysis has been presented to determine effective length factor for models composed of gusset plate and bracing members. The direct calculation was not possible for complex geometries such as gusset plate and steel braces. The results of the analysis indicated substantial differences attributable to gusset plate detailing, even if the length of the brace tube is identical. Thick and large gusset plates restricted brace buckling while more compact and thinner gusset plates may enhance overall effective length, leading to reduce buckling strength. The actual effective length of gusset plate and bracing members lies between the two extremes of the brace models with idealized pinned and rigid connections end conditions. A good comparison between the hysteresis loops of the FE models and test models supports the effectiveness and accuracy attributable to the finite element framework that was developed explicitly in this study. Particularly, comparing predicted to test values, the mean ratio and Cov on average were 1.14 and 0.18 for yield load, 1.11 and 0.15 for ultimate load, 1.14 and 0.15 for initial buckling load, 1.03 and 0.23 for energy dissipation capacity and 0.91 and 0.06 for ultimate ductility capacity, respectively.

The FE models confirmed the experimental findings and validated the connection design methods by examining local strain measurements, lateral displacement outputs, cycles to global and local buckling, including fatigue-life. The FE model and test results endorse the balanced design method for delivering consistently greater energy dissipation capacity, including fatigue lives with improvement. While comparing models of Tremblay (2002) and Goggins (2004) for predicting post-buckling strength, the predictions mainly were below the results obtained from tests and FE models, specifically at ductility of 4. Moreover, models of predicting lateral deformation were compared with results of FE models and found that the model of Tremblay (2002) gave overestimated prediction, while the model of Hassan *et al*. (2015) gave relatively better predictions. The comparison of the observed and predicted peak ductility capacities with models of Nip *et al*. (2010) and Tremblay (2002) indicated that the former model is conservative over the range of slenderness investigated, while the latter model gave relatively close prediction for specimens with lower slenderness, but overestimated predictions for larger slenderness.

The current study contributes to the need for information on detailing and modelling gusset plates and bracing members by engineers who look for guidance on realistic structural details involving economy. The FE and test results presented in this paper allows further investigation of these observations, including the study of various parameters influencing response of CBF structure under cyclic axial loading, such as during earthquakes.

Acknowledgments

References

ABAQUS (2013), *Analysis User's Manual I-V, Version 6.13*, ABAQUS, Inc., Dassault Systémes, U.S.A.

Bjorhovde, R. and Chakrabarti, S. (1985), "Tests of full-size gusset plate connections", *J. Struct. Eng.*, **111**(3), 667-684.

Broderick, B.M., Goggins, J., Beg, D., Elghazouli, A.Y., Mongabure, P., Le Maoult, A., Hunt, A., Salawdeh, S., Moze, P. and O'Reilly, G. (2015), "Assessment of the seismic response of concentrically-braced steel frames", *Exp. Res. Earthq. Eng.*, Springer, Berlin, Germany.

Brown, V.L.S. (1989), "Stability of gusseted connections in steel structures", Ph.D. Dissertation, University of Delaware, U.S.A.

Eurocode (1993), Eurocode 3: Design of steel structures - Part 1-1: General rules and rules for buildings, European Committee for Standardization (CEN); Brussels, Belgium.

Eurocode (2004), Eurocode 8 : Design of Structures for earthquake resistance Part 1: General rules, seismic actions and rules for buildings, European Committee for Standardization (CEN); Brussels, Belgium.

Chaboche, J.L. (1986), "Time independent constitutive theories for cyclic plasticity", *J. Plasticity*, **2**(2), 149-188.

Cheng, J.J.R., Yam, M.C.H. and Hu, S.Z. (1994), "Elastic buckling strength of gusset plate connections", *J. Struct. Eng.*, **120**(2), 538-559.

Coffin, L. (1954), "A study of the effect of cyclic thermal stresses on a ductile metal", *Trans. ASME*, **76**, 931-950.

ECCS (1986), "Recommended testing procedure for assessing the behaviour of structural steel elements under cyclic loads", *ECCS Technical Committee 1, Structural Safety and Loadings, Technical Working Group 1.3, Seismic Design*, ECCS, Brussels, Belgium.

English, J. and Goggins, J. (2012), "Nonlinear seismic response of concentrically braced frames using frames using finite element models", *15th World Conference on Earthquake Engineering,* Lisbon, Portugal, September.

Fell, B.V. (2008), "Large-scale testing and simulation of earthquake-induced ultra low cycle fatigue in bracing members subjected to cyclic inelastic buckling", University of California, Davis, MA, U.S.A.

Gardner, L., Saari, N. and Wang, F. (2010), "Comparative experimental study of hot-rolled and cold – formed square and rectangular hollow sections", *Thin-Walled Struct.*, **48**(7), 495-507.

Goggins, J. (2004), "Earthquake resistance hollow and filled steel braces", Ph.D. Dissertation, Trinity College, University of Dublin, Ireland.

Goggins, J., Broderick, B.M., Elghazouli, A.Y., Salawdeh, S., Hunt, A., Mongabure, P. and English, J. (2018), "Shake table testing of concentrically braced steel structures with realistic connection details subjected to earthquakes", *Structures*, **13**, 102-118.

Goggins, J. and Salawdeh, S. (2013), "Validation of nonlinear time history analysis models for single-storey concentrically braced frames using full-scale shake table tests", *Earthq. Eng. Struct. Dynam.*, **42**(8), 1151-1170.

Goggins, J.M., Broderick, B.M., Elghazouli, A.Y. and Lucas, A.S. (2006), "Behaviour of tubular steel members under cyclic axial loading", *J. Construct. Steel Res.*, **62**(1-2), 121-131.

Haddad, M. (2015), "Concentric tubular steel braces subjected to seismic loading: Finite element modelling", *J. Construct. Steel Res.*, **104**, 155-166.

Haddad, M., Brown, T. and Shrive, N. (2004), "Fintie element modelling of concentriccally braced frames for earthquakes", *13th World Conference on Earthquake Engineering*, Vancouver, Canada, August.

Hassan, M.S., Goggins, J. and Salawdeh, S. (2015), "Charactersing the effect of global and local geometric imperfections on the numerical performance of a brace member", *J. Physics: Conference Series*, **628**(1), 012063.

Hassan, M.S., Salawdeh, S. and Goggins, J. (2018), "Determination of geometrical imperfection models in finite element analysis of structural steel hollow sections under cyclic axial loading", *J. Construct. Steel Res.*, **141**, 189-203.

Hu, S. and Cheng, J.J.R. (1987), "Compressive behavior of gusset plate connections", Structural

Engineering Rep. No. 153; University of Alberta, Canada.

Hunt, A.D. (2013), "Design and analysis of concentrically braced steel frames under seismic loading". Ph.D. Dissertation, Trinity College Dublin, Dublin, Ireland.

Kavinde, A.M. and Deierlein, G.G. (2004), "Micromechanical simulation of earthquake-induced fracture in steel structures", Report no.145; Stanford University, San Francisco, California.

Lehman, D.E., Roeder, C.W., Herman, D., Johnson, S. and Kotulka, B. (2008), "Improved seismic performance of gusset plate connections", *J. Struct. Eng.*, **134**(6), 890-901.

Manson, S.S. (1953), "Behaviour of materials under conditions of thermal stress", *Heat Transfer Symposium*, University of Michigan Engineering Research Institute, Michigan, U.S.A.

Nip, K.H., Gardner, L., Davies, C.M. and Elghazouli, A.Y. (2010), "Extremely low cycle fatigue tests on structural carbon steel and stainless steel", *J. Construct. Steel Res.*, **66**(1), 96-110.

Nip, K.H., Gardner, L. and Elghazouli, A.Y. (2010), "Cyclic testing and numerical modelling of carbon steel and stainless steel tubular bracing members", *Eng. Struct.*, **32**(2), 424-441.

Nip, K.H., Gardner, L. and Elghazouli, A.Y. (2013), "Ultimate behaviour of steel braces under cyclic loading", *Proc. Inst. Civil Eng. - Struct. Build.*, **166**, 219-234.

Palmgren, A. (1924), "Die Lebensdauer von Kugellagern (The life of roller bearings)", *Zeitschrift des Vereines Deutscher Ingenieure*, **68**(14), 339-341.

Rudland, D.L. and Brust, F. (1997), "The effect of cyclic loading during ductile tearing on the fracture resistance of nuclear pipe steels", *Fatigue Fracture Mech*, **27**, 406-426.

Ryan, T., Broderick, B.M., Hunt, A., Goggins, J. and Salawdeh, S. (2017), "Recommendations for numerical modelling of concentrically braced steel frames with gusset plate connections subjected to earthquake ground motion", *J. Struct. Integrity Maintenance*, **2**(3), 168-180.

Salawdeh, S., English, J., Goggins, J., Elghazouli, A.Y., Hunt, A. and Broderick, B.M. (2017), "Shake table assessment of gusset plate connection behaviour in concentrically braced frames", *J. Construct. Steel Res.*, **138**, 432-448.

Salawdeh, S. and Goggins, J. (2013), "Numerical simulation for steel braces incorporating a fatigue model", *Eng. Struct.*, **46**, 332-349.

Tremblay, R. (2002), "Inelastic seismic response of steel bracing members", *J. Construct. Steel Res.*, **58**(5-8), 665-701.

TK

Appendix

Table A1 Symbols and nomenclature

Lower case	
a	Parameter of a nonlinear regression equation
b	Brace width
b_1	Parameter of a nonlinear regression equation
b_w	Whitmore width
b_{iso}	Hardening parameter that defines the rate at which the size of the yield surface changes as plastic strain increases
c	Parameter of a nonlinear regression equation
f_y	Yield strength of brace material
$f_{y,g}$	Yield strength of gusset plate
k	Effective buckling length factor
l_h	Width of gusset plate
l_v	Depth of gusset plate
n_i	Number of reversals for which the strain level is applied
t	Thickness of brace section
t_p	Thickness of gusset plate

Upper case	
A	Cross-sectional area of brace section
$A_{net,brace}$	Net brace area for gusset plate connection
C	Fatigue ductility exponent
C_{kin}	Kinematic hardening parameter
Cov	Coefficient of variation
DI	Damage index
E	Modulus of elasticity
F_c	Initial buckling capacity of brace member
F_y	Initial yield capacity of brace member
F_u	Ultimate load capacity of brace member
$F_{y,gusset}$	Yield capacity of gusset plate
L_b	Length of brace
N_{cr}	Elastic critical buckling load
N_{fi}	Number of reversals causing failure at a specific strain level
Q_∞	Maximum change in the size of the yield surface
$R_{y,brace}$	Ratio of actual to nominal yield strength of brace
$R_{y,gusset}$	Ratio of actual to nominal yield strength of gusset plate
SPOS	Section positive (point of integration of shell element)
W_{total}	Total energy dissipated

Table A1 (continued)

Greek upper case	
β	Ratio of global imperfection magnitude, ω_1 and brace tube length, L_b
β_{ww}	Balanced factor for balanced design
γ	Parameter that determines the rate at which the back stresses vary as the plastic strain increases
Δ	Lateral deformation
ε'_f	Fatigue ductility coefficient
$\dfrac{\Delta\varepsilon_p}{2}$	Plastic strain amplitude
εy	Yield strain of material
$\bar{\lambda}$	Global normalised slenderness
σ_{cr}	Plate critical buckling stress
$\sigma|_o$	Yield stress at zero equivalent plastic strain

Greek Lower case	
α	Imperfection factor
δ_c	Applied displacement magnitude
δy	Yield displacement
ω_1	Global imperfection amplitude
ω_2	Local imperfection amplitude
δ	Ultimate displacement